THE ASTROPHYSICAL JOURNAL, 437:239–261, 1994 December 10

VIOLENT STAR FORMATION IN NGC 2363

ROSA M. GONZÁLEZ-DELGADO,[1] ENRIQUE PÉREZ,[1,2] GUILLERMO TENORIO-TAGLE,[1] JOSÉ M. VILCHEZ,[1]
ELENA TERLEVICH,[3,4] ROBERTO TERLEVICH,[3] EDUARDO TELLES,[3] JOSÉ M. RODRÍGUEZ-ESPINOSA,[1]
MIGUEL MAS-HESSE,[5] MARÍA LUISA GARCÍA-VARGAS,[6] ÁNGELES I. DÍAZ,[6]
JORDI CEPA,[1] AND HECTOR CASTAÑEDA[1]
Received 1994 February 18; accepted 1994 June 1

ABSTRACT

We present narrowband Hα imaging and long-slit optical and near-infrared spectroscopy of the giant H II region NGC 2363. The spectroscopic data are taken at two positions, in the brightest core and in a knot ~6″ to the east, where we have found broad emission lines at 4660 Å and 5810 Å attributed to WC stars which suggest an age for the region between 3 and 5 Myr. The observations also confirm previously reported low-intensity broad components in Hα and [O III] emission lines, which extend some 500 pc across the region. For 15 different zones within the nebula, we derive the physical conditions and the chemical abundance of oxygen, nitrogen, neon, sulfur, and helium. No significant spatial variations are found for these abundances, with a mean value of oxygen $12 + \log(\mathrm{O/H}) = 7.89$ and a helium mass fraction of $y = 0.24$. Electron temperatures deduced from the Paschen discontinuity have been obtained for two different regions. These Paschen temperatures are significantly smaller than those obtained from the collisionally excited emission line diagnostics, suggesting the presence of large temperature fluctuations. The effect of these temperature fluctuations in the determination of the chemical abundances has been estimated.

Subject headings: H II regions — ISM: abundances — ISM: individual (NGC 2363) — stars: Wolf-Rayet

1. INTRODUCTION

Given the present knowledge of stellar evolution and of the physics of ionized nebulae, one can conclude without a doubt that H II regions are among the best indicators of the conditions that lead to massive star formation. This is because what H II regions show us are the cloud properties immediately after the moment of star formation. Giant extraglactic H II regions, in particular, display the conditions that have led to violent bursts of stellar formation and given their luminosity and age; from them one is led to realize which properties of the parent cloud(s) and the local sectors of galactic disks gave origin to violent stellar bursts.

This is the first of a series of papers presenting the results obtained by the GEFE[7] collaboration. The principal goal of GEFE is to determine the various factors or physical properties that control the efficiency of large-scale star formation. For this, instead of the usual practice of attempting to correlate the column density of matter (either H I, or H_2, or the sum of both, even if they are clearly totally unaware of star formation) with the degree of importance of well-localized star formation events, the collaboration has carried out a systematic study of the ionization, density structure, metallicity, temperature, gas-to-dust ratio, and dynamics of extragalactic H II regions.

High spatial resolution information about the density structure is needed in order to determine accurately the ionization structure of giant H II regions. Together with the temperature, these are the main properties that one needs to know in order to derive chemical abundances. All this information may be obtained by long-slit spectroscopy over selected areas in each region. One can also derive gas velocity dispersions to ascertain the dynamical stage of these violent star-forming regions.

Two important aspects of the GEFE program are emphasized in this paper; one is related to the determination of chemical abundances in giant H II regions and H II galaxies. These abundances affect the stellar evolution (e.g., stellar winds) and perhaps star formation via the initial mass function. The other aspect concerns the study of the kinematical state of these regions of violent star formation where photoionization and the huge amount of mechanical energy dumped into the interstellar medium by stellar winds and supernova explosions affect the cloud structure and eventually cause the disruption of the leftover gas.

One of the targets of the GEFE program is the giant H II region NGC 2363 located at the south west of the irregular galaxy NGC 2366. It is one of the largest extragalactic H II regions with high surface brightness. Hα imaging shows a large shell surrounding the region. Roy et al. (1991), using a Fabry-Perot interferometer, found [O III] line splitting in the brightest core of the region, consistent with a giant shell of ionized gas 285 pc in diameter, expanding with a velocity of 45 km s^{-1}. More recently, Roy et al. (1992) have reported the discovery of low-intensity broad components in the Hα and [O III] emission lines. They measure a full width at half-maximum (FWHM) of the [O III] broad component of 40 Å and find it to be extended some 500 pc toward the east. The nature of this high-velocity gas remains unknown.

[1] Instituto de Astrofísica de Canarias, 38200 La Laguna, Tenerife, Spain.
[2] Present address: Instituto de Astrofísica de Andalucía, Apdo. 3004, 18080 Granada, Spain.
[3] Royal Greenwich Observatory, Madingley Road, Cambridge CB3 0EZ, UK.
[4] Present address: Institute of Astronomy, Madingley Road, Cambridge CB3 0HA, UK.
[5] Laboratorio de Astrofísica Espacial y Física Fundamental (LAEFF), Apdo. 50727, 28080 Madrid, Spain.
[6] Departomento Física Teórica CIX, Universidad Autónoma, Cantoblanco, 28049 Madrid, Spain.
[7] GEFE (Grupo de Estudios de Formación Estelar) is an international collaboration of astronomers from Spain, the United Kingdom, France, Germany, Denmark, and Italy, formed to take advantage of the international time granted by the Comité Científico International at the Observatories in the Canary Islands.

The optical and radio study of this region (Kennicutt, Balick, & Heckman 1980) shows that NGC 2363 presents an unusually high degree of excitation and a very low dust content. The authors estimated a lower limit of 10^3 O6 V stars required to account for the Hα luminosity. They further suggest that the properties of the NGC 2363 complex closely resemble those of Markarian galaxies.

Peimbert, Peña, & Torres-Peimbert (1986) determined the chemical composition of NGC 2363 from an integrated spectrum corresponding to an aperture of 3″.8 × 12″.4 oriented east-west. They found a C/O ratio 2 times smaller than in the solar vicinity, a N/H ratio 17 times smaller than in the Orion Nebula, and an He/H abundance of 0.077.

In this paper, we present narrowband Hα imaging and long-slit spectrophotometry from 3700 to 9600 Å in two locations in the region, at the brighest knot (henceforth knot A) and at 6″ to the east, knot B (see Fig. 2). We study spatially the main physical properties of the gas, such as reddening, electron densities, temperature, and chemical composition. We confirm the existence of a broad low-intensity component in [O III] and Hα and report the existence of W-R features in emission at 4660 and 5810 Å in knot B.

2. OBSERVATIONS AND DATA REDUCTION

2.1. *Optical Imaging*

Narrowband CCD images of NGC 2363 were taken during three observing runs, in 1991 December and in 1992 January and November, with the 1 m Jacobus Kapteyn Telescope on the Roque de Los Muchachos Observatory in La Palma. For the first two runs we used a 400 × 590 pixel GEC CCD as a detector; this provides a total field of 2′ × 3′ with a scale of 0.3 arcsec pixel^{-1}. A 1180 × 1280 pixel EEV chip was used in the last run, with a field of 5′.9 × 6′.4 and 0″.3 pixel^{-1}. Images through interference filters, FWHM = 50 Å, centered at 6563 Å for Hα and at 6832 Å for the continuum, were obtained. The software package FIGARO, as provided by Starlink, was used to reduce the data following the standard procedure of subtracting the bias and dividing by a normalized flat field. Spectroscopic standard stars were observed through the same filters and used for flux calibration. No continuum was removed from the on-band image to produce a pure Hα image because the total underlying continuum emission amounts to less than 1% of the Hα flux. A final image (Fig. 1) was obtained by adding to the individual exposures, after alignment by means of three stars in the field. A journal of observations is given in Table 1.

2.2. *Optical and Near-Infrared Spectroscopy*

Spectroscopic observations were obtained with the 4.2 m William Herschel Telescope at the Roque de los Muchachos Observatory, during two runs in 1992 February and October, using the blue and red arms of the ISIS double spectrograph and an EEV CCD chip in each arm. Two different gratings were used, R316 in the red arm and R300 in the blue arm, covering a spectral range from [O II] λ3727 to [S III] λ9532 in three different spectral ranges of about 1700 Å each. The dispersion of 1.4 Å pixel^{-1} with the slit width used of 1″.2 gives an effective spectral resolution of about 3 Å. The size of the CCD along the spatial direction was reduced to 3′, with a spatial sampling of 0″.3 pixel^{-1} in the February run and 0″.6 pixel^{-1} in the October run. The slit was set in two different locations (see Fig. 2). In February it was located across the brightest knot (knot A) at a position angle (P.A.) = 187° and at 6″ to the east of this (knot B) at P.A. = 130°; both position angles coincide with the paralactic angle. During the October run, the slit was placed across knot B at P.A. = 185° (paralactic angle) and P.A. = 130° (not paralactic). The seeing was around 1″.2 during the two runs. The journal of these observations is also shown in Table 1.

TABLE 1

JOURNAL OF OBSERVATIONS

Date	P.A.	Wavelength (Å)	Time (s)	Comments
1991 Dec 24	...	6563	1800	Hα image
1991 Dec 24	...	6832	1800	Continuum
1991 Dec 26	...	6563	1800	Hα image
1991 Dec 26	...	6832	1800	Continuum
1992 Jan 12	...	6563	2 × 1800	Hα image
1992 Dec 12	...	6832	1800	Continuum
1992 Nov 8	...	6563	2 × 1800	Hα image
1992 Nov 8	...	6832	2 × 1800	Continuum
1992 Feb 26	187°	5900–7550	300	Knot A
1992 Feb 26	187	5900–7550	3 × 600	Knot A
1992 Feb 26	187	3680–5400	300	Knot A
1992 Feb 26	187	3680–5400	3 × 600	Knot A
1992 Feb 26	187	3680–5400	2 × 1800	Knot A
1992 Feb 26	187	7890–9500	2 × 1800	Knot A
1992 Feb 26	130	3680–5400	2 × 1800	Knot B
1992 Feb 26	130	7890–9500	2 × 1800	Knot B
1992 Oct 23	130	3710–5430	2 × 1800	Knot B
1992 Oct 23	130	5310–6960	2 × 1800	Knot B
1992 Oct 23	185	3710–5430	900	Knot B
1992 Oct 23	185	5310–6960	900	Knot B

The data were reduced using the FIGARO data processing software. Bias and flat-fielding were performed in the usual way. A two-dimensional wavelength calibration was done using the program ARC2D (Wilkins & Axon 1991) by fitting a third-order polynominal to the position of the lines in the calibration lamp frames, the rms deviation from the fits was less than 0.1 Å, except for the blue spectra in the February run, when it was 0.3 Å. The spectra were corrected for atmospheric extinction using a mean extinction curve appropriate for La Palma Observatory (King 1985). The frames were flux-calibrated with spectroscopic flux standard stars observed during the same night with a 4″.5 wide slit. Only one standard was observed for the red and IR range in each night, while for the blue range in the February run, three standard stars were observed, and in this case, the agreement between the individual calibration curves was better than 5%.

The curves given by Filippenko (1982) were used to predict displacements due to differential refraction, both parallel and perpendicular to the slit, as a function of wavelength and air mass. All the frames with displacements along the slit larger than a third of a pixel were corrected. Since the observations have been done at paralactic angle (except for P.A. = 130° in the October run), no displacements perpendicular to the slit (along the spectral direction) were found. These corrections were performed in the two-dimensional frames by means of a special purpose program which corrects each pixel according to the value appropriate for the corresponding wavelength (as given by Filippenko 1982). As a check of the atmospheric differential refraction correction, in Figure 3 we show the blue spectrum of the central 2″ in knot B. The spectra taken at paralactic angle are basically identical and are different from the spectrum at P.A. = 130° taken during the October run,

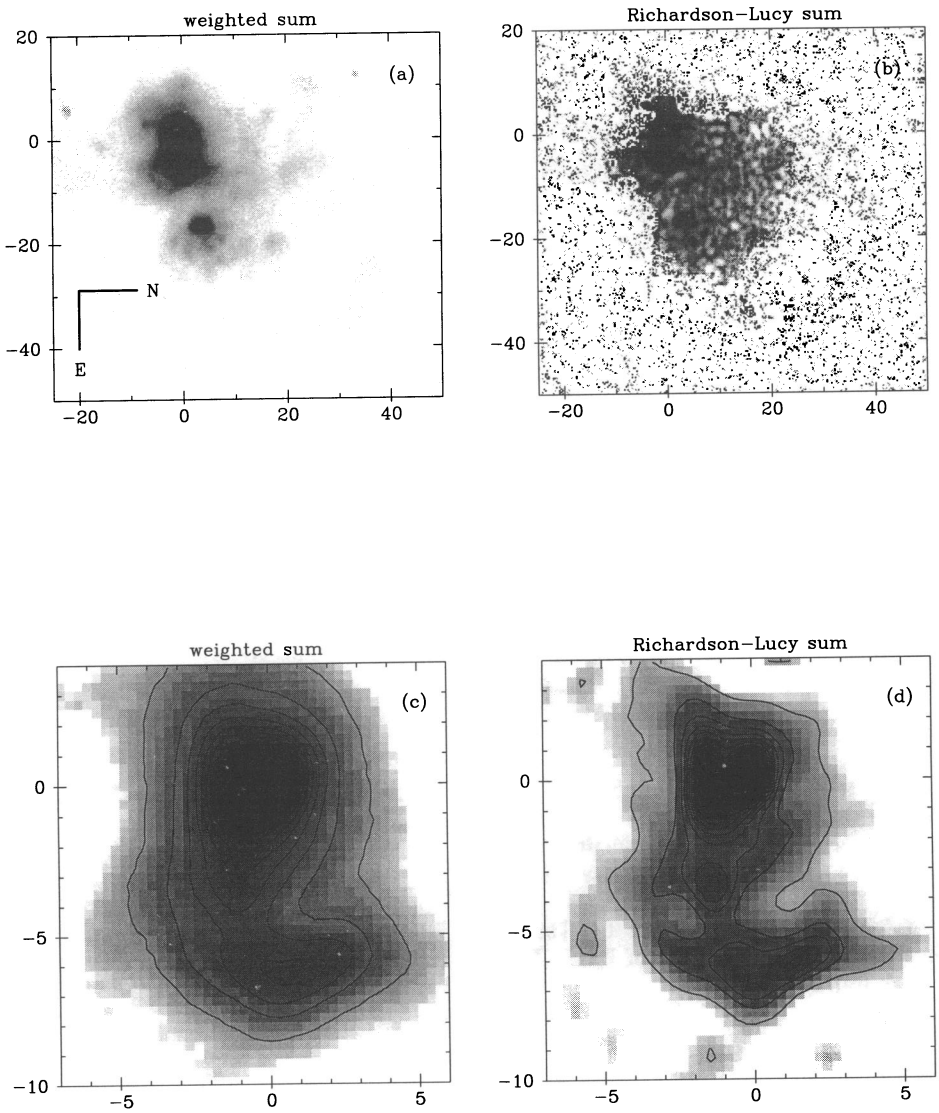

FIG. 1.—Hα image after co-adding four independent frames: (*a*) with a weighted sum and (*b*) using the Richardson-Lucy algorithm for image deconvolution. In (*b*) the very low surface brightness in the north-east quadrant is clearly visible. The internal structure of NGC 2363 is expanded in the bottom panels, (*c*) and (*d*). North is to the right, and east down. The axes are in arcseconds taking the maximum emission (knot A) as the origin. Spatial sampling is 0".3 pixel^{-1} and 1" = 17.9 pc. In (*a*) the length of the orientation bars is 200 pc each.

which was observed 80° off paralactic. The latter data (P.A. = 130°) are used independently from those taken at paralactic angle and are so indicated whenever used.

Since the nebular emission is extended and fills most of the slit length, sky subtraction was performed in every data frame using the outermost increments. Prior to sky subtraction each frame was flattened along the spatial direction by dividing by polynomial fits to the spatial profile of the sky light distribution. Finally, after sky subtraction, a spatial alignment was performed prior to co-adding all frames of the same position angle and wavelength range taken in the same epoch.

3. ANALYSIS OF THE Hα IMAGES

The analysis of the Hα images was performed after a reddening correction corresponding to $E_{B-V} = 0.15$ mag, obtained from the spectroscopic data.

Figure 1 shows the Hα map of the complex formed by NGC 2366 I and II. This complex comprises NGC 2366 I (NGC 2363), NGC 2366 II, and a very low surface brightness shell-like extension into the northeast quadrant. Of the total flux in the complex of 9.8×10^{-12} ergs s^{-1} cm^{-2} (see below for a description of the measuring method), 88% (8.7×10^{-12} ergs s^{-1} cm^{-2}) corresponds to NGC 2363, while 12% (1.1×10^{-12} ergs s^{-1} cm^{-2}) corresponds to NGC 2366 II and the shell-like component.

Figure 1 shows the result of adding all the frames taken in different epochs in two different ways. In Figure 1*a*, a weighted sum of all the frames has been performed, using the signal-to-noise ratio of each image. In Figure 1*b* the frames have been added by using the Richardson-Lucy algorithm, to sum frames with different point-spread functions (PSFs), as implemented in the IRAF software package task ACOADD (Richardson 1972; Lucy 1974; Hook & Lucy 1992). Figures 1*c* and 1*d* are the corresponding panels for an enlargement of NGC 2363. The two main components seen in the weighted sum image (Fig. 1*c*), correspond to knots A and B as studied below with the spectroscopic data. After the Richardson-Lucy co-addition it is possible now to resolve NGC 2363 into four main components.

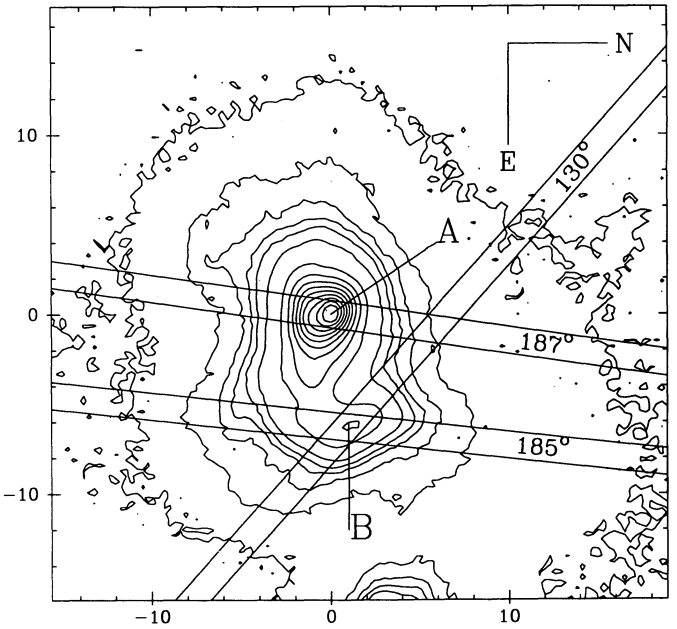

FIG. 2.—Contour plot of the Hα image showing the slit positions used for the spectroscopic observations. Knot A was observed at P.A. = 187°, and knot B at P.A. = 185° and 130°. The length of the orientation bars is 100 pc each.

These include knot A, resolved into a compact bright core and a fainter component 1″.3 to the south, knot B, 6″ to the east with a head-tail structure, and an additional component 3″ east of knot A, which is only seen as an extension in the weighted sum image.

The input for the ACOADD task consists of the list of frames to be added plus the corresponding list of PSFs. The PSF was obtained for each frame by fitting a Moffat function (Moffat 1969; Terebizh 1990) to the azimuthal averaged radial profile of two or three stars within the frame. For the different stars, the agreement between the two free parameters in the fitted function was good, and a mean value was used to construct an analytical PSF for each frame. Different number of iterations were used to check the quality of the co-added image, with no significant improvement found after about 50 iterations.

Rather than using a fixed-shape aperture, to perform flux measurements we used a special algorithm that measures the flux within a given isophotal contour level. The contour level is specified and the region where the measurements are to be made is isolated by hand, then the algorithm searches for all the pixels where the flux is larger than or equal to the specified level. The output is the total flux and the precise area where it has been measured. In fact, the routine allows any number of contour levels to be measured simultaneously, and thus contour photometry can be easily performed.

The total flux measured for NGC 2363 within the contour level corresponding to 1.1×10^{-16} ergs s^{-1} cm^{-2} pixel^{-1}, after correcting for $E_{B-V} = 0.15$ mag (as obtained below from the spectroscopy), is 8.7×10^{-12} ergs s^{-1} cm^{-2}. This flux translates to an Hα luminosity of 1.4×10^{40} ergs s^{-1} at a distance of 3.7 Mpc. The number of 0″.3 × 0″.3 image pixels contributing to the flux is 6720, so if we define the effective radius of the region as $(\mathrm{Area}/\pi)^{1/2}$, this number corresponds to a radius of 250 pc.

This lead to an estimate of the rms electron density, $\langle N_e \rangle_{\mathrm{rms}}$, such that

$$\langle N_e \rangle_{\mathrm{rms}}^2 = \frac{Q(\mathrm{H}^0)}{\alpha_B(\mathrm{H}^0, T)V},$$

where $Q(\mathrm{H}^0)$ is the ionizing photon luminosity, which can be obtained from the Hα luminosity given above as 1.5×10^{52} photons s^{-1}, and V is the ionized volume of the region. Using $R = 250$ pc radius, we obtain $\langle N_e \rangle_{\mathrm{rms}} = 5.5$ cm^{-3}, which in conjunction with the mean electron density (190 cm^{-3}) obtained in § 4.3 gives a value of 0.8×10^{-3} for the overall filling factor of NGC 2363. A more detailed study of the structure derived from the Hα images of NGC 2363 and other giant extragalactic H II regions will be given in a forthcoming paper (Pérez et al. 1994).

4. SPECTROSCOPIC RESULTS

Figures 4 and 5 show the two-dimensional frames in the three spectral ranges for knot A (P.A. = 187°) and for knot B (P.A. = 130°). At both locations, the Hα and [O III] emission extends 90″, some 60″ from the core to the north and 30″ to the south of the maximum.[8] The stellar light is more concentrated in the central 15″ around the core. The very broad component discovered by Roy et al. (1992) can be clearly appreciated as a fuzzy halo around [O III] in Figure 4. To perform the analysis of the physical conditions, several one-dimensional spectra have been extracted to improve the signal-to-noise ratio of the data. These comprise four spectra for the brighest knot A, and five spectra at each position angle for the eastern knot B. The details of the extraction are summarized in Table 2 and also shown in Figure 8.

The merged spectra for the highest signal-to-noise extractions are shown in Figures 6 and 7, for knots A and B, respectively. These figures are shown in two different intensity scales so that the weakest lines are better appreciated. Both positions display more than 20 lines of the hydrogen Paschen series, including the series limit, a prominent nebular He II λ4686 and low-intensity broad components in Hα and [O III]. Knot B

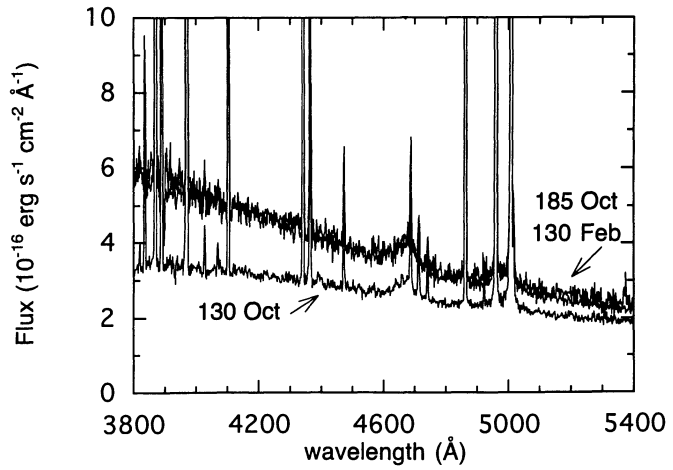

FIG. 3.—Central 2″ spectrum for knot B, at P.A. = 130° (February and October runs) and P.A. = 185°. The effect of the atmospheric differential refraction can be seen as a change in the continuum level.

[8] Scales in arcseconds are positive from the knot maximum toward the north.

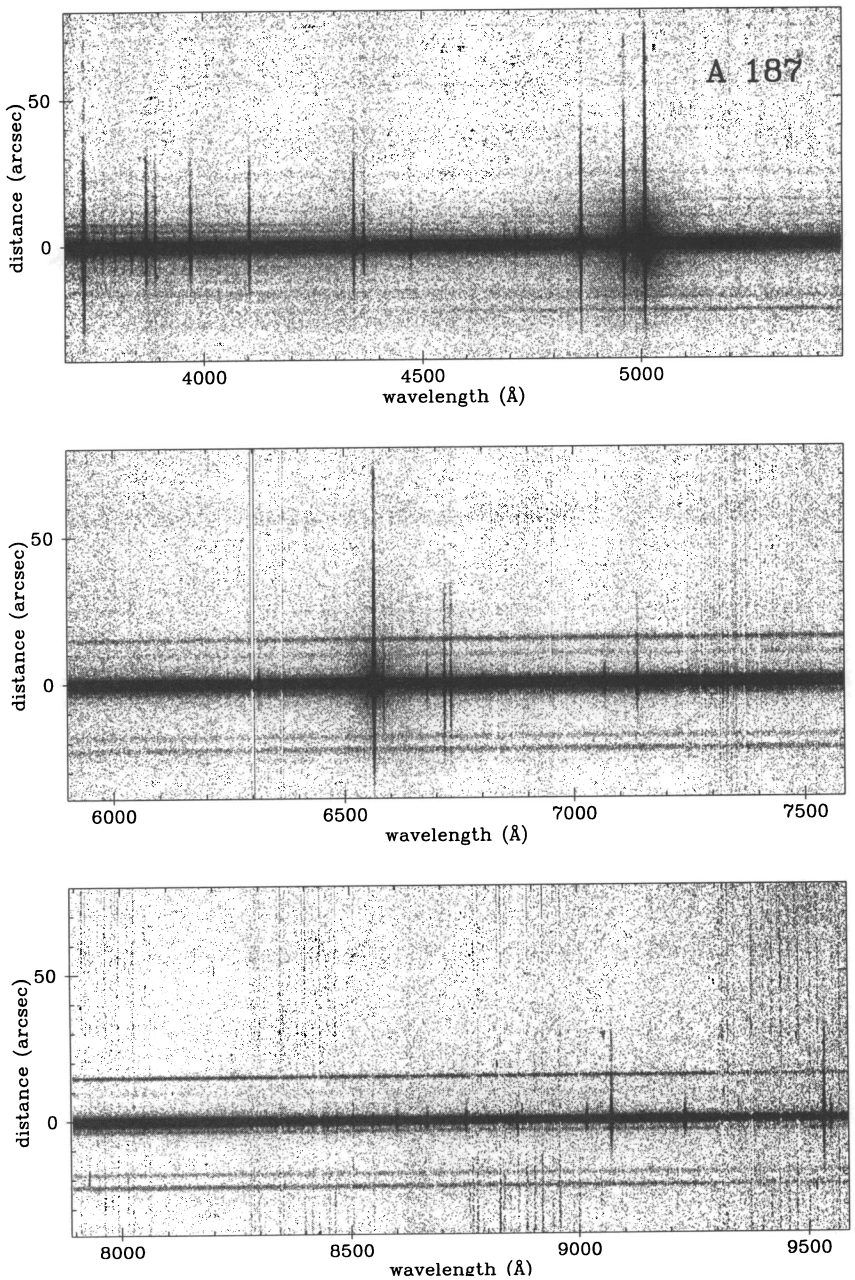

FIG. 4.—Two-dimensional frames in the three spectral ranges for knot A, at P.A. = 187°. North is up. Note the presence of broad components under [O III] seen as a fuzz extended on both sides of the maximum.

TABLE 2

EXTRACTION OF ONE-DIMENSIONAL SPECTRA

	Spectrum					
Knot	1	2	3	4	5	6
Knot A	A1 −15″.8 −5″.9	A2 −5″.9 9″.1	A3 9″.1 15″.4	A4 15″.4 27″.4		
Knot B (P.A. = 130°, Oct)	B1 −10.5 −3.3	B2 −3.3 2.1	B3 2.1 5.1	B4 5.1 7.5	B5 7″.5 20″.3	WR 130 −0″.3 2″.1
Knot B (P.A. = 130°, Feb)	C1 −10.2 −3.3	C2 −3.3 2.1	C3 2.1 5.1	C4 5.1 7.5	C5 7.5 20.3	
Knot B (P.A. = 185°, Oct)	D1 −16.5 −4.5	D2 −4.5 2.1	D3 2.1 5.7	D4 5.7 17.1	D5 17.1 35.1	WR 185 0.3 2.7

NOTE.—The two numbers give the extracted window for each spectrum. Origin is taken at the maximum of line emission.

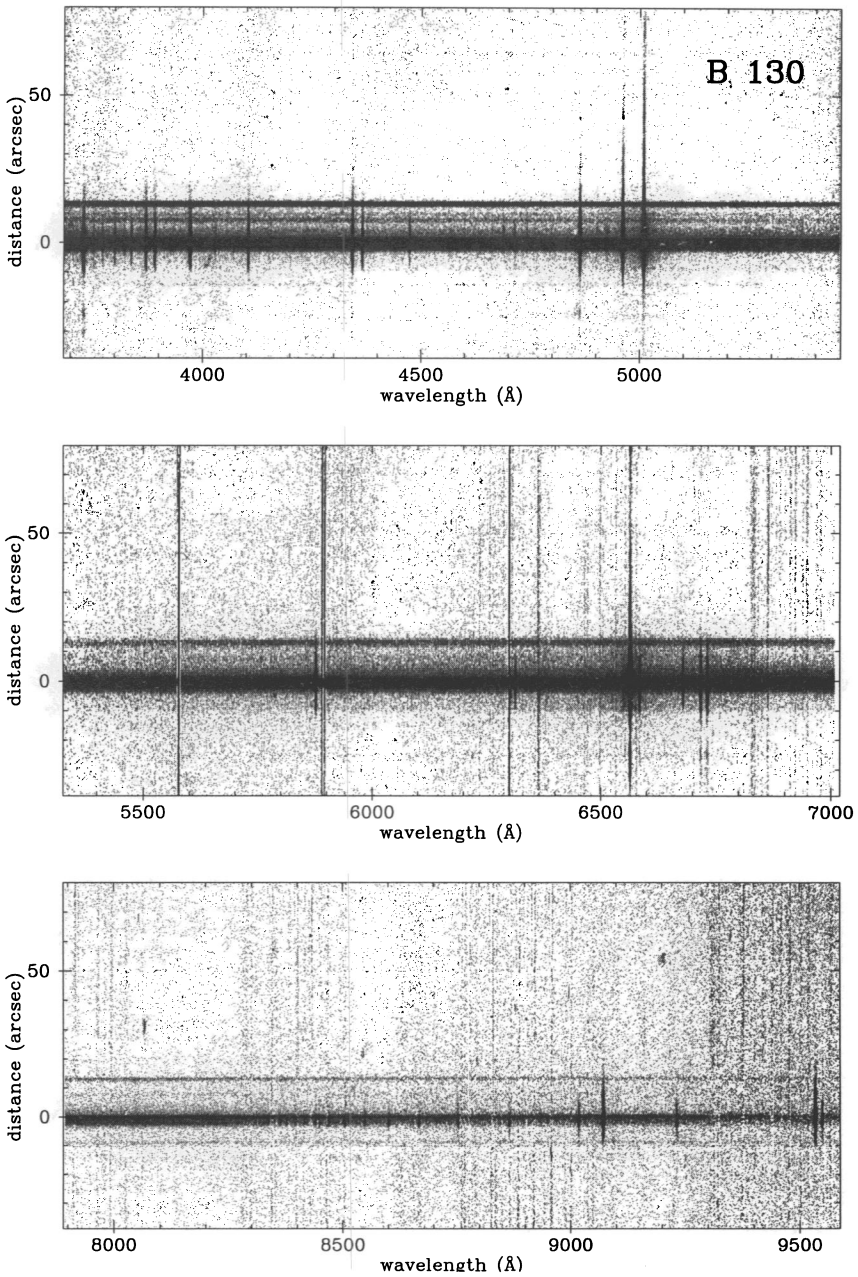

FIG. 5*a*

FIG. 5.—Two-dimensional frames in the three spectral ranges for knot B at (*a*) P.A. = 130°, northwest direction up, and (*b*) P.A. = 185°, north is up

features clear WR bumps at 4660 Å and 5810 Å. Both knots present very high excitation spectra, which is also reflected in both positions by the weak [N II] λλ6548, 6584 lines in the wings of Hα. The spectra of the central core for each knot show that the excitation of the brightest knot A is higher than that of knot B, except for the nebular He II λ4686. The continuum is also flatter for knot A, as can be expected for a higher excitation H II region.

4.1. *Spatial Distribution of the Emission Lines*

The spatial distributions of the emission lines [O III] λ5007, Hα, and [S III] λ9532 are quite similar. These are shown in Figure 8. The continuum (extracted from the range λλ5054–5064) and the emission lines peak at the same position for knot A; however, for knot B, the peak of the continuum is shifted 1″.2–1″.5 to the north with respect to the peak of the emission lines. The distribution of the emission lines for P.A. = 185°, knot B, is double peaked, and the maximum of the continuum is located between the two peaks. All of the spatial profiles indicate that the emission lines extend further toward the north.

The distribution of the excitation, [O III] λ5007/Hβ (Fig. 9), for the two knots is qualitatively similar. It shows a steep fall to the south and a shallower decrease toward the north. For knot

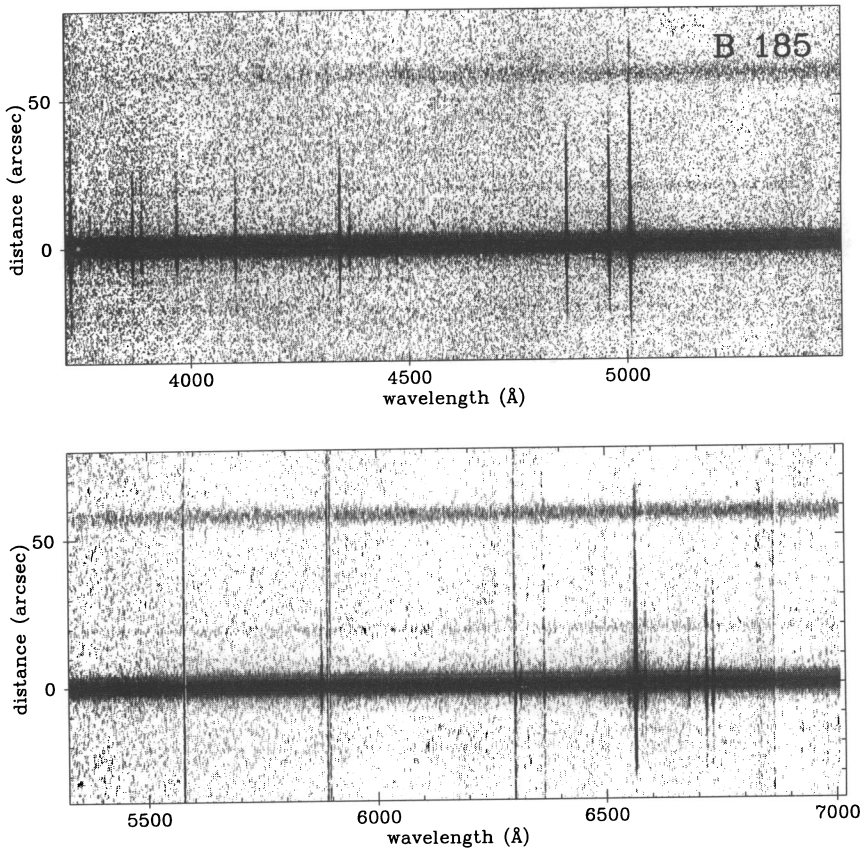

FIG. 5b

B, the distribution shows a plateau extending about 20″ north of the peak emission, which coincides with the faint halo emission visible in the Hα image of Figure 1.

The [O III]/[O II] distributions (Fig. 10) follow closely those of the excitation parameter. In P.A. = 130°, this ratio has a maximum about 6″ north of the peak emission. At the maximum of knot A, this ratio is about twice as large as for knot B.

Because the continuum spatial profile is narrower than the emission line one, the distribution of the equivalent width shows a double peak (Fig. 11), with a local minimum coinciding with the maximum of the continuum emission. At this central minimum the equivalent widths of Hα for knots A and B are 1500 Å and 600 Å, respectively. We note that the largest equivalent width does not coincide with the maximum emission line brightness; it is displaced ~2″ to the south in the three position angles.

4.2. *Line Intensities*

Line intensities for all the identified emission lines in each spectrum have been measured using the Starlink package DIPSO (Howarth & Murry 1991). The measurement is carried out by summing all the flux densities across the line profile above the local mean continuum level. To check the reliability of the line intensities, we have made a comparison between the intensities measured at P.A. = 130° in the February (at paralactic angle) and October (off paralactic) runs for knot B; typical differences amount to less than 10%. This sets an upper limit to the uncertainty in our measurements.

As mentioned above, the [O III] λλ4959, 5007 and Hα lines show in some of the spectra a low-intensity broad component; the flux of these broad lines was obtained by fitting Gaussian profiles. A narrow component was first fitted in order to obtain the flux of the narrow lines, and then a broad component was fitted to the residual.

The observed line intensities were corrected for reddening according to the standard reddening curve (Whitford 1958) and assuming theoretical values for the Balmer and Paschen decrements corresponding to case B recombination (Brocklehurst 1971). The reddening constant $C(\mathrm{H}\beta)$ was deduced by fitting a slope to the ratio of the observed to the theoretical value versus the reddening curve. A low value, $C(\mathrm{H}\beta) \sim 0.2$, was found for every spectrum, with no significant variation of the reddening across the region. Table 3 lists for each spectrum the reddening-corrected line intensities normalized to Hβ. The equivalent width (which is not corrected for reddening) and flux of Hβ are also included. The values of $C(\mathrm{H}\beta)$ for each spectrum extracted are given in last column of Table 4.

The errors in the line fluxes have been computed from the expression $\sigma_l = \sigma_{\mathrm{cont}} N^{1/2}[1 + \mathrm{EW}(N\Delta)^{-1}]^{1/2}$, where σ_l is the error in the line flux, σ_{cont} represents the standard deviation in a continuum window near the emission line measured, N is the number of pixels used in measuring the line flux, EW is the line equivalent width, and Δ is the dispersion in Å pixel^{-1}. The first term represents the error in the line flux introduced by the uncertainty in placing the continuum level, while the second term scales the signal-to-noise ratio (S/N) of the continuum to the line. The errors associated to each line flux measurement are propagated in quadrature when calculating all the sub-

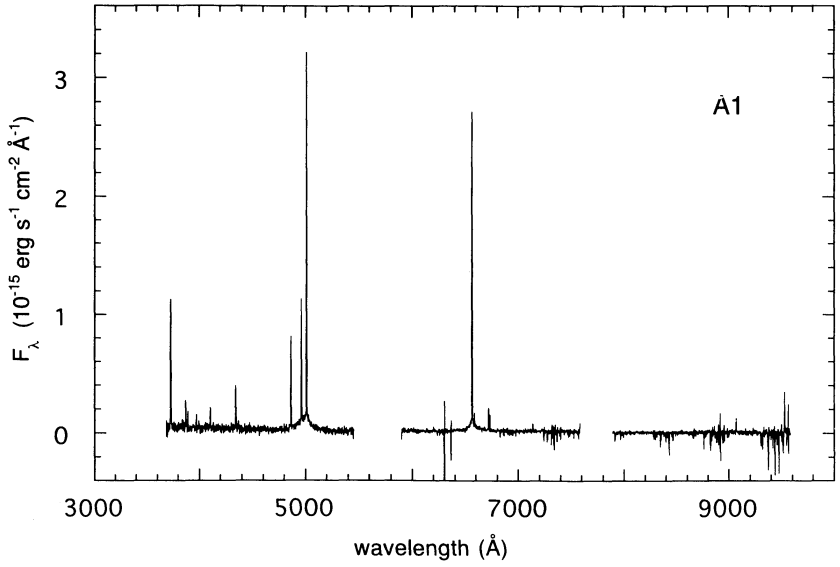

FIG. 6*a*

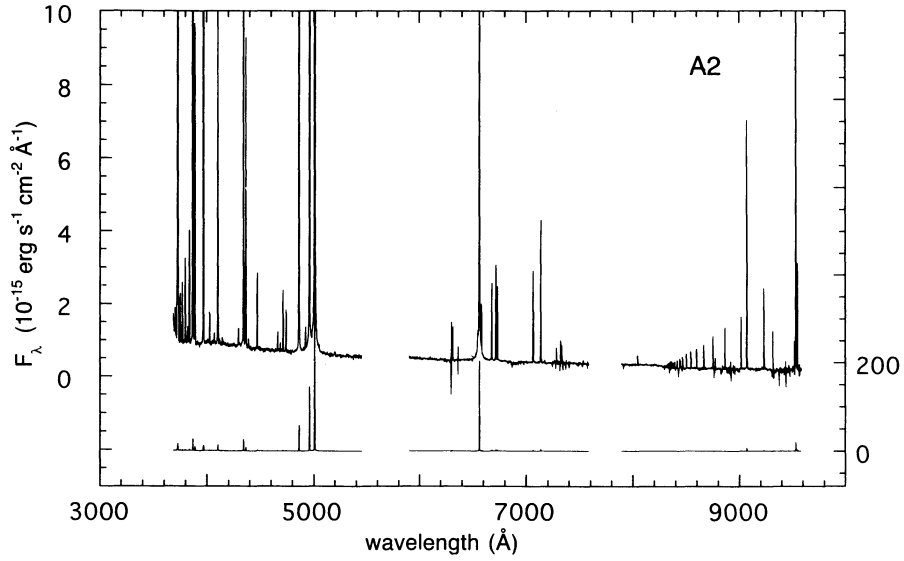

FIG. 6*b*

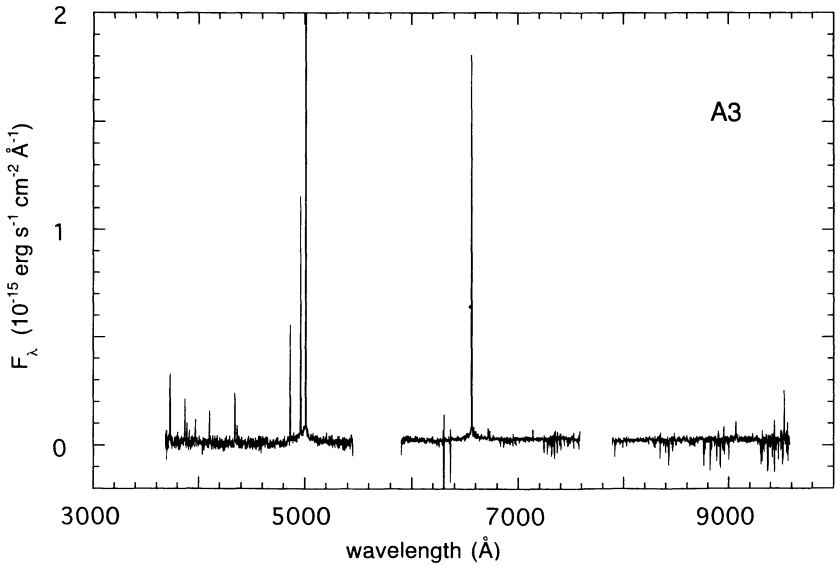

FIG. 6*c*

FIG. 6.—Merged spectrum for knot A (with two intensity scales), at P.A. = 187°, and the cross sections (*a*) A1, (*b*) A2, and (*c*) A3 as described in Table 12 and indicated in Fig. 8. The spectra shown are not correct for reddening.

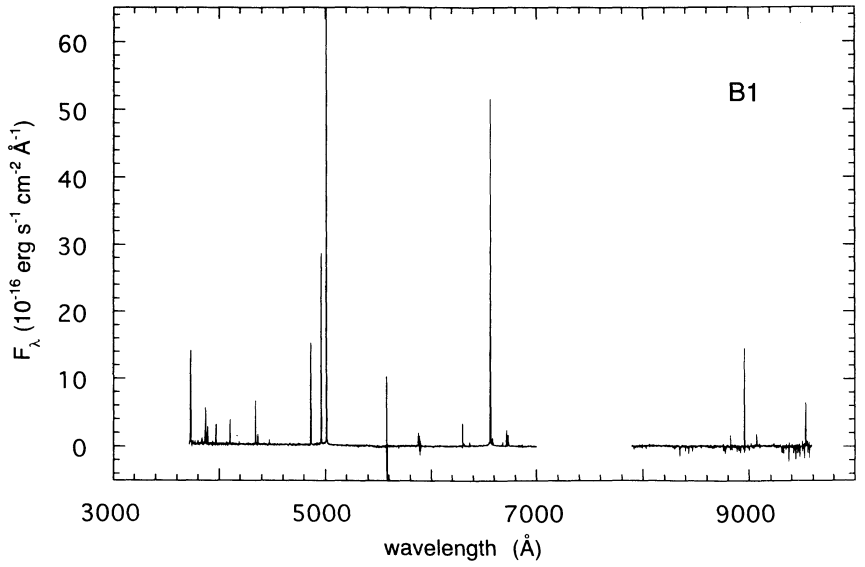

FIG. 7*a*

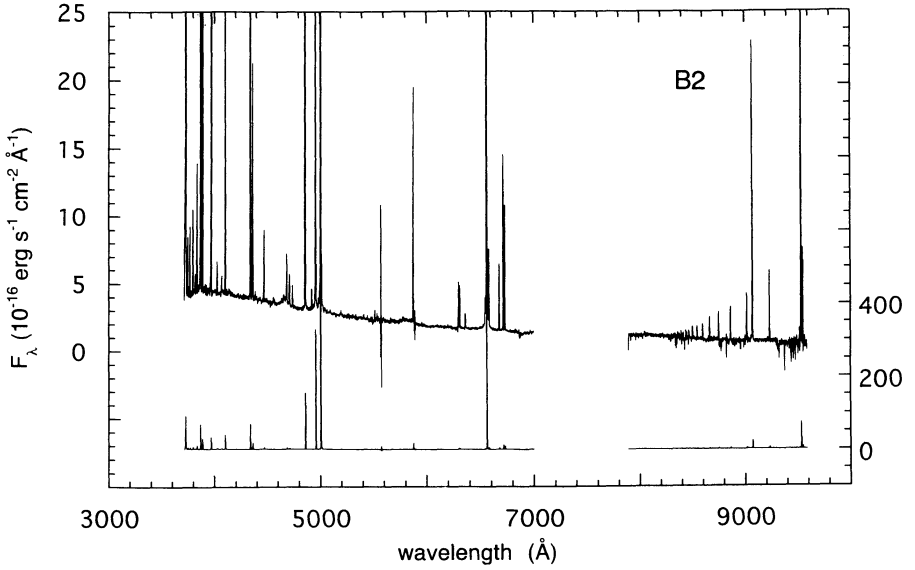

FIG. 7*b*

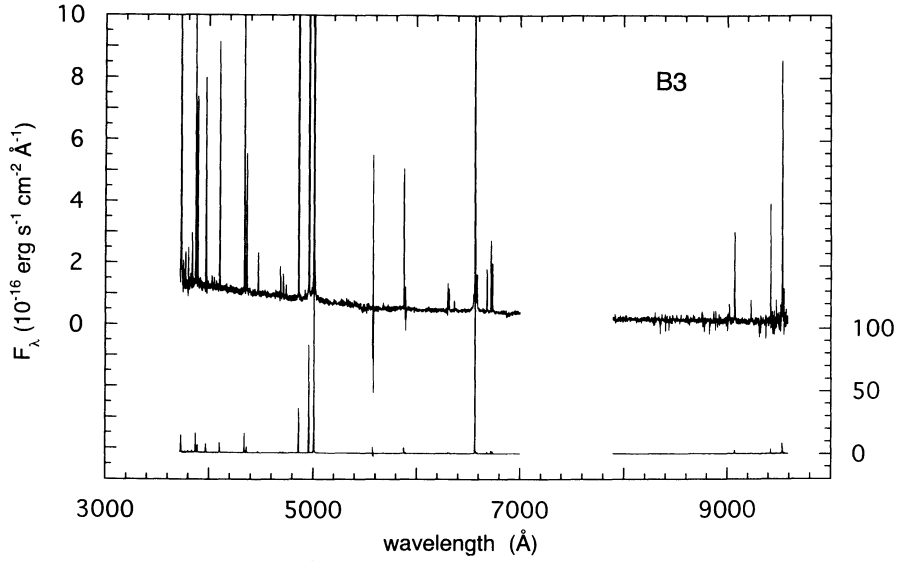

FIG. 7*c*

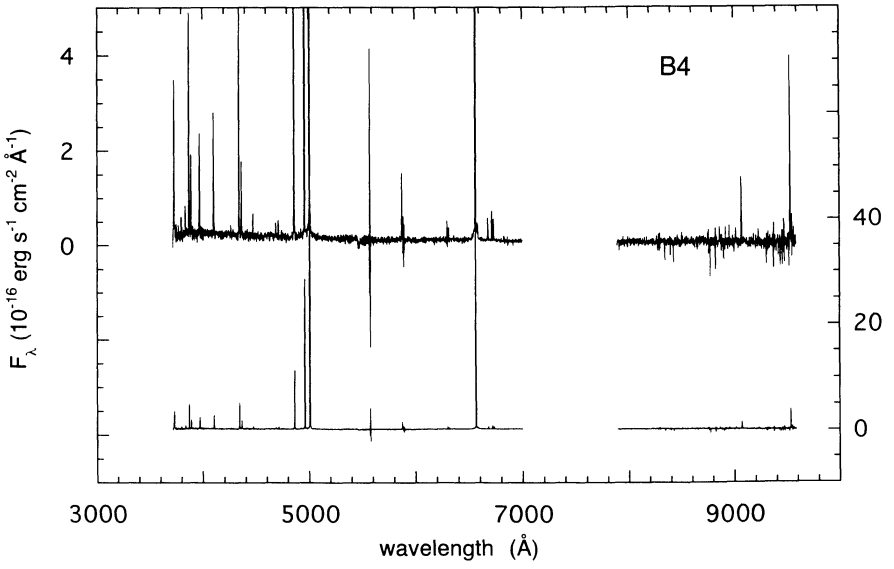

FIG. 7*d*

FIG. 7.—Merged spectrum for knot B (with two intensity scales), at P.A. = 130°, and the cross sections (*a*) B1, (*b*) B2, (*c*) B3, and (*d*) B4; and for knot B, at P.A. = 185°, and cross sections (*e*) D1, (*f*) D2, (*g*) D3, and (*h*) D4. The spectra shown are not corrected for reddening.

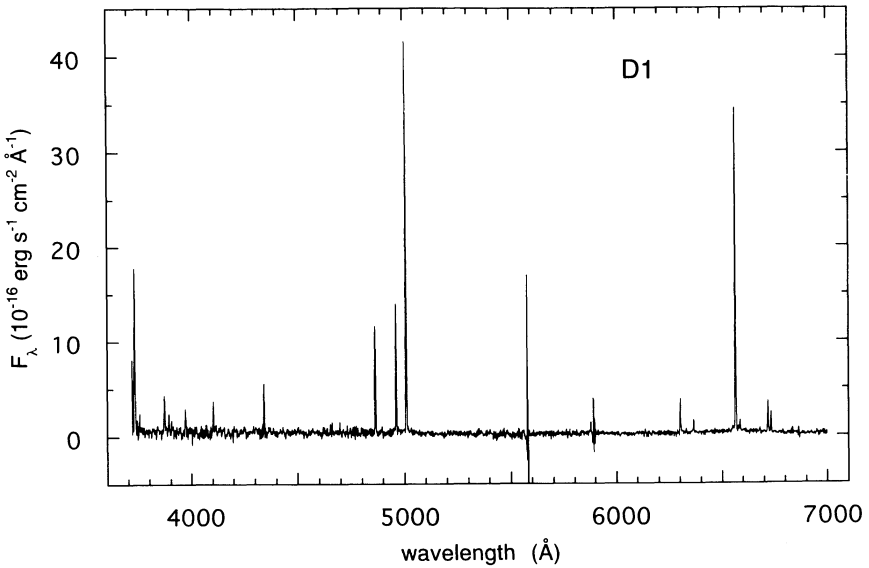

FIG. 7*e*

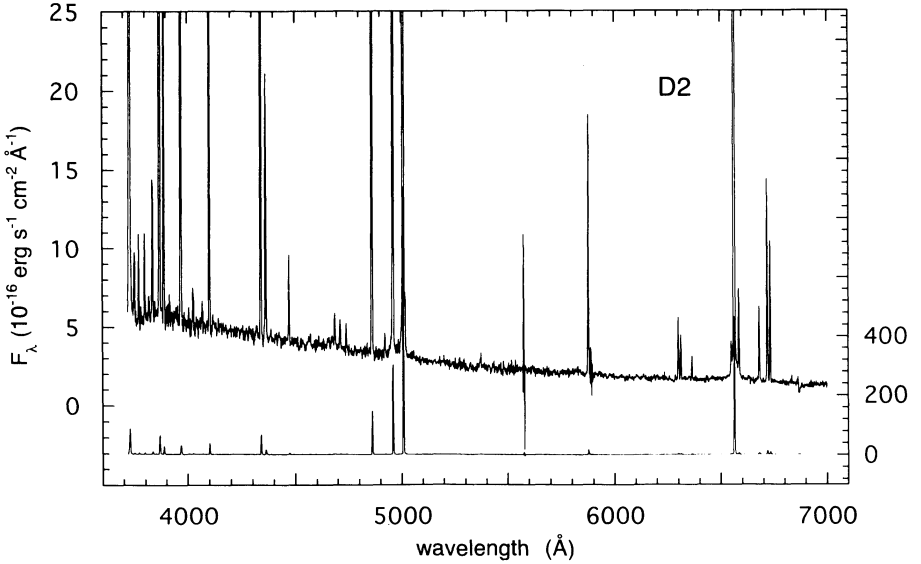

FIG. 7*f*

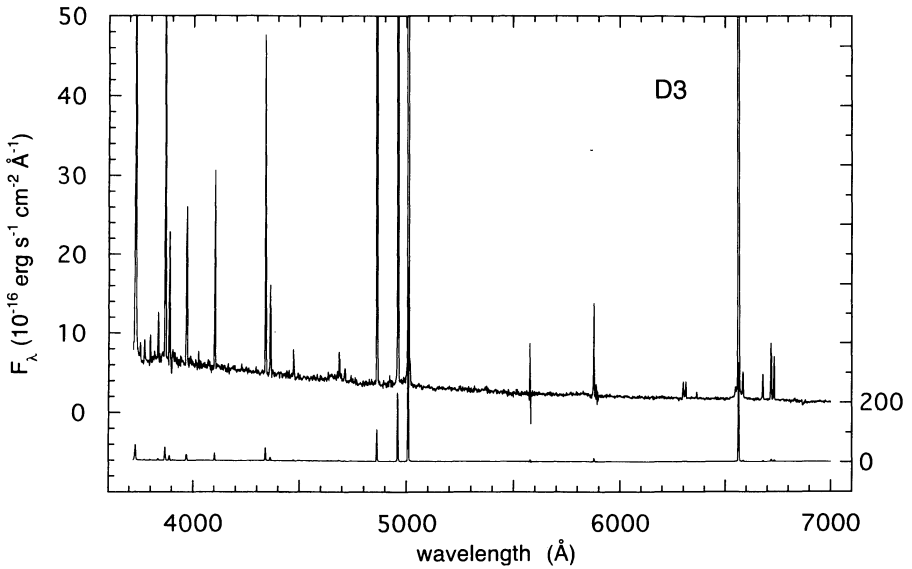

FIG. 7*g*

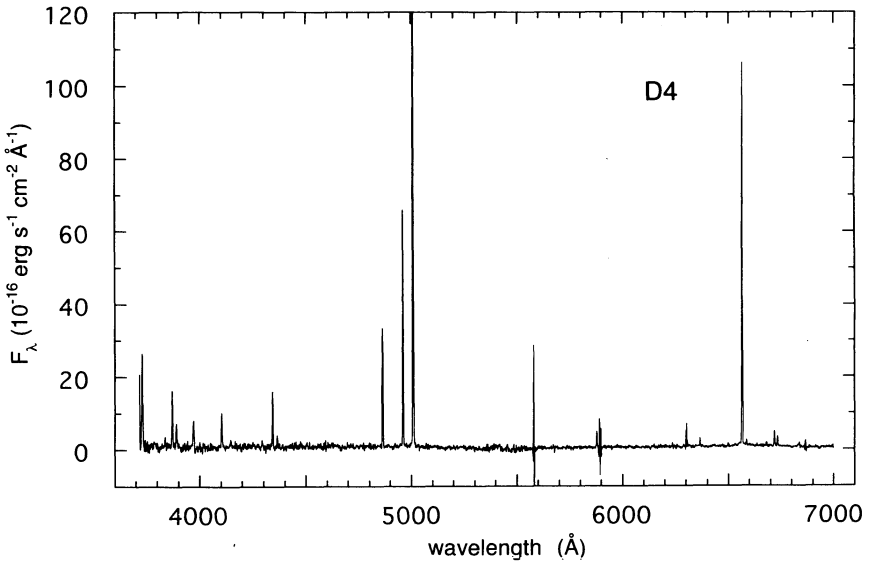

FIG. 7*h*

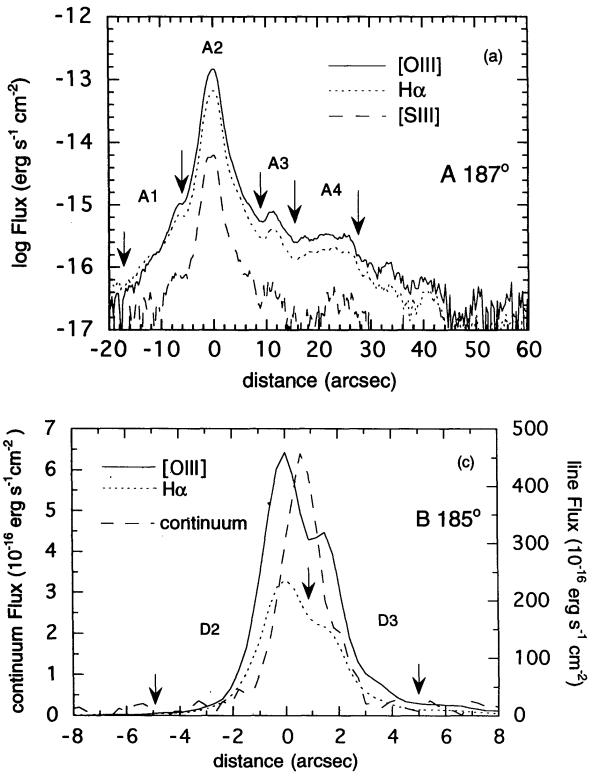

FIG. 8.—Spatial distributions (not corrected for reddening) of the emission lines [O III] λ5007, Hα, and [S III] λ9532 for knot A and [O III] λ5007, Hα, and continuum (extracted from the window 5054–5064) for knot B. Arrows mark the positions where the spectra have been extracted. (*a*) In knot A the maxima of the emission lines are aligned with the maximum of the continuum distribution. (*b*) and (*c*) In knot B, the maximum of the continuum is shifted 1″.2 to the north. The W-R features are detected at the maximum of the continuum. The origin of the horizontal axis is coincident with the maximum of the emission lines.

sequent quantities, such as the line ratios. For a spectrum with a continuum with S/N ≥ 10 (e.g., A2, B2, and D2) the errors in the line fluxes are quite small (less than a few percent), smaller than the uncertainties introduced in the measuring process; but for spectra with S/N ~ 4 (e.g., B1 and B4) the error for the brightest lines rises to nearly 10%, and close to 20% for weaker lines.

4.3. *Electron Densities and Temperatures*

Gas densities were calculated from the [S II] λ6717/λ6731 ratio using the expression given by McCall (1984). Individual values are given in Table 4. The weighted mean value obtained is ~189 cm^{-3}, with no significant variations or gradient, within the errors, across the region. The electron temperature was determined from the line ratios [O III] λ4363/λλ(5007 + 4959), [S II] λλ(4068 + 4073)/λλ(6717 + 6731), and [S III] λ6312/λλ(9069 + 9532), following the expressions proposed by Seaton (1975) and Aller (1984) with the atomic parameters given by Mendoza (1983). For the central core of knot A (spectrum A2), it was also possible to calculate the electron temperature from the line ratio [O II] λλ(7320 + 7330)/λ3727. For knot B, we combine the near-infrared data at P.A. = 130° from the February run with the red data from the October run also at P.A. = 130°, to obtain the [S III] temperature.

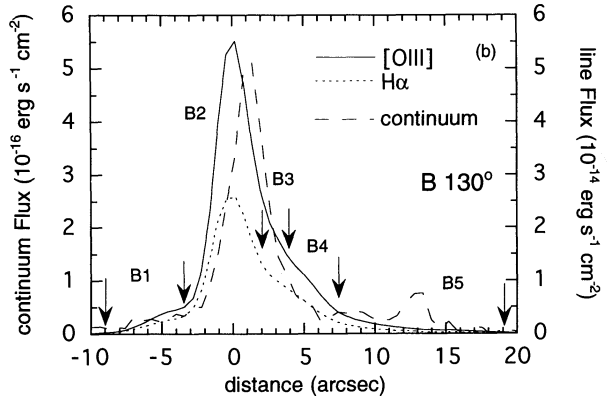

The differences between T_e([O III]) and T_e([S III]) are between 5% and 10%, except for the low signal-to-noise spectrum, for which it is nearly 20%. Given the large uncertainties associated to T_e([S III]), these differences are within the calculated errors, but *all* the values of T_e([S III]) are systematically larger.

The values of T_e([O III]) found for knots A and B were ~16,000 K and 15,000 K, respectively. No significant gradient in T_e([O III]) was found.

The value T_e([O II]) = 14,500 ± 1300 K in A2 was obtained. Since only for A2 was it possible to calculate T_e([O II]), we have used Stasińska's (1982) expression, $t(O^+) = 0.7t(O^{+2}) + 0.3$, where t is the temperature in units of 10^4 K, for the computation of the low-ionization ionic abundances.

4.4. *Ionic and Total Abundances*

Ionic and total abundances for the elements O, Ne, N, S, and He were calculated from their corresponding line intensity ratios and the adopted electron temperatures and densities, using the standard expressions (e.g., Pagel et al. 1992).

We estimate that the contribution of the O^{+3} to the total abundance of oxygen is less than 5%. If the sulfur abundance is calculated using for S^{+2} the optical or the infrared lines, the value can change between 1% and 17% (depending on the signal-to-noise ratio of the spectrum), but this discrepancy in the sulfur abundance depending on the line chosen is always smaller than its computed error.

In high-excitation H II regions, a considerable fraction of the sulfur is ionized beyond the S^{+2} stage. Garnett (1989) has modeled the ionization correction factor ($ICF = 1 + S^{+3}/(S^+ + S^{+2}) = S/(S^+ + S^{+2})$) for S for low-abundance objects, and he finds that for nebulae ionized by stars with effective temperatures higher than 40,000 K, the ICF is nearly independent of the ionization parameter and the effective temperature, and it can be calculated as a function of the O^+/O fraction. In the range of O^+/O values that we measure, Garnett's model can be approximated by Stasińska's (1978) formula with $\alpha = 2.5$:

$$\frac{S^+ + S^{+2}}{S} = \left[1 - \left(1 - \frac{O^+}{O}\right)^{\alpha}\right]^{1/\alpha}.$$

Table 5A includes the ICF calculated in this way. The values found are in the range 1.3–2.2. Figure 12 shows how the sulfur abundance values obtained for the different regions are independent of excitation, as represented by the line ratio [O III] λ5007/[O II] λ3727, consistent with the ICF values used.

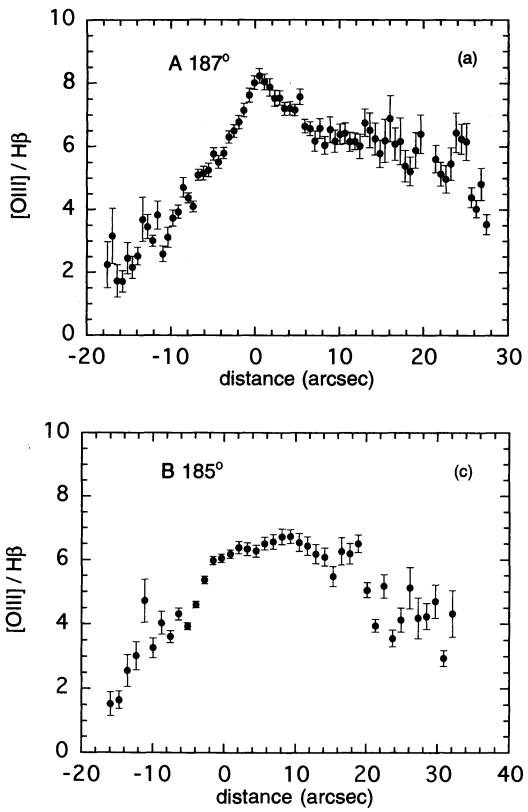

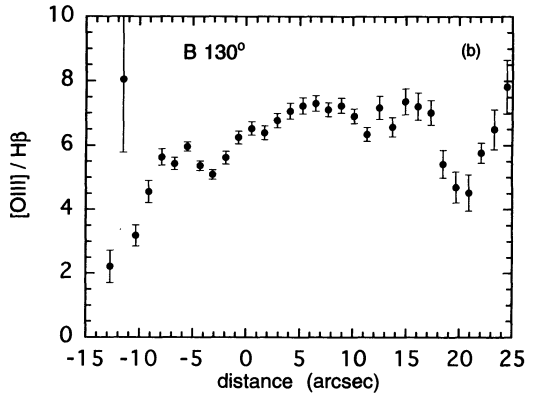

FIG. 9.—As in Fig. 8, for the ratio [O III] $\lambda5007/H\beta$. Note the steep fall of the excitation to the south and a shallower decrease to the north.

At both locations, in knots A and B, He II $\lambda4686$ was detected to be very extended, so we calculate the He abundance, assuming that there is no contribution from He^0, as

$$\frac{He}{H} = \frac{He^+ + He^{+2}}{H^+} .$$

As an additional check, we have calculated the parameter $\eta = (O^+/O^{+2})/(S^+/S^{+2})$ (Vilchez & Pagel 1988). The values found are $\log \eta < 0$, which, using the calibration given by Vilchez (1987) for the ICF and η, imply an ICF = 1, which justifies our assumption regarding the correction from He^0.

For the determination of He^+/H^+ (Table 5B), we have used the He I lines at $\lambda4471$ and $\lambda6678$ for knot A, and $\lambda4471$, $\lambda5876$, and $\lambda6678$ for knot B. The fluxes in these lines were converted to abundance values using the theoretical emissivities of Brocklehurst (1971).

For high electron temperatures, as in the case of NGC 2363, the effect of collisional excitation in the level population of He I could be important. We have estimated the correction to the He I line strength for the contribution from collisional excitation, using the expression given by Clegg (1987), and have corrected it according to Peimbert & Torres-Peimbert (1987) and R. E. S. Clegg (1994, private communication). The ratio of excitations by collisions to those by recombination is $\sim$1.5% for $\lambda4471$ and $\sim$4% for $\lambda5876$. Since for our case corrections are close to the uncertainties that we have in the determination of the He^+ abundance (after the error propagation), we have not performed any correction for collisional excitation.

An additional correction to the He^+ abundance which might be considered is that caused by the underlying stellar absorption. However, we have neglected this correction after checking that the flux ratio of $\lambda4922/\lambda4471$ has approximately its expected theoretical value of 0.3. Further support comes from Figure 13, where we show that the ionic abundance of He^+ calculated using $\lambda4471$, $He^+(4471)/H^+$, does not depend on EW(Hβ), indicating that underlying stellar absorption is not important and that the value obtained for the He abundance is very solid. The equivalent width of He^+ $\lambda4471$ in absorption for a variety of star clusters is always smaller than 0.3 Å (Olofsson 1989), which implies an upper limit of 2% and 4% of the emission line equivalent width, for knots A and B, respectively; this is within the errors, and in any case it goes in the sense that compensates the collisional excitation effects, which are of the same order of magnitude.

No significant variations of the chemical abundances were found across the region. The values are shown in Table 5C. The oxygen abundance is roughly one-ninth of the solar value, and the nitrogen is 25 times smaller than solar. These values are 7% and 30% smaller than the values obtained by Peimbert et al. (1986). It is possible that their larger value of N/H might be due to contamination of the broad Hα emission underlying their measurements of [N II] $\lambda\lambda6548, 6583$.

The mean value of sulfur abundance is 38% smaller than the value obtained by Peimbert et al. (1986). This difference is mainly caused by the fact that they used a higher value for the ICF, equal to 2.2, instead of the values adopted here (Table 5A).

The mean log (S/O) value is -1.71, equal to the solar value, and log (N/O) = -1.61 equals the value obtained by Skillman & Kennicutt (1993) for IZw18.

Table 5C also includes the weighted mean abundances for knot A, for knot B, and for the whole region NGC 2363.

4.5. *The W-R Feature*

Wide bumps in emission centered at 4660 Å (width $\sim$70 Å) and at 5810 Å (width $\sim$80 Å) were detected in the central part of knot B. These features are usually attributed to atmospheric emission in W-R stars. In addition, narrow nebular lines are superimposed, including He II $\lambda4686$ and [Ar IV] $\lambda\lambda4711, 4740$ on the 4660 Å bump, and He I $\lambda5876$ on the 5810 Å one.

Because these W-R features are faint, no individual stellar lines have been detected in the 5810 Å blend, but C IV $\lambda4658$ seems to be present in the 4660 Å blend. Figure 14 shows the two bumps and also indicates the position of other stellar lines, such as N III $\lambda\lambda4642, 4634$ and N V $\lambda\lambda4620, 4604$.

The feature at 5810 Å and the C IV $\lambda4658$ line could be attributed to WC stars. WC stars are expected from the evolution of stars with masses higher than 60 $M_\odot$ at ages between 3

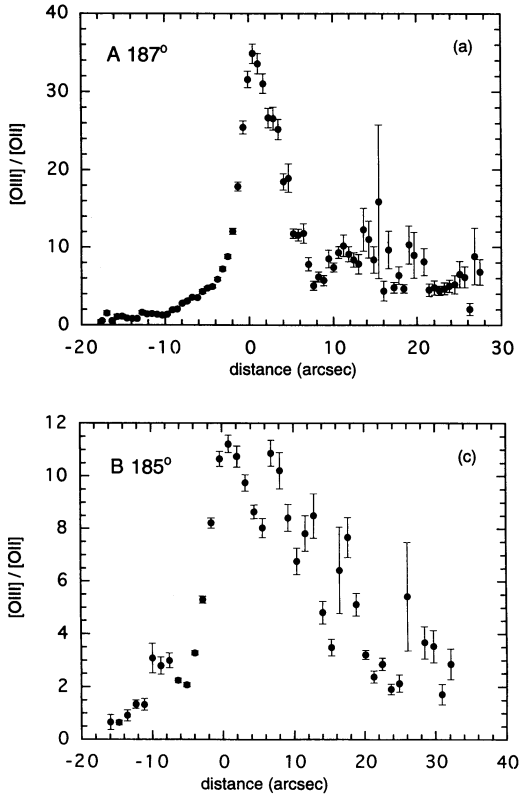

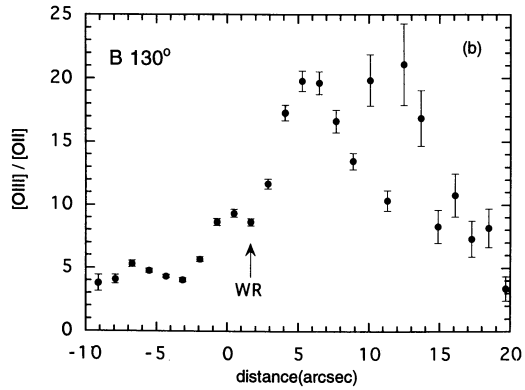

FIG. 10.—As in Fig. 8, for the ratio [O III] λ5007/[O II] λ3727. The maximum is coincident with the maximum emission for knot A; however, for knot B, it is at 6″ to the north.

and 5 Myr, for a cluster of 0.2 solar metallicity (Fogotto et al. 1994).

The emission line blend was measured by fitting a Gaussian profile after subtracting the narrow component for the emission lines He II λ4686, [Ar IV] λλ4711, 4740, and He I λ5876. The flux, equivalent width, and luminosity of the bumps, assuming a distance of 3.7 Mpc, are given in Table 6.

From the calculated luminosities one can estimate the number of W-R stars present in the ionized nebulae. One can for example use the calibration given by Smith (1991). Smith estimates that a single WC4 star has a luminosity of $10^{36.5}$ ergs s^{-1} in the 5810 Å bump and $10^{36.7}$ ergs s^{-1} in the 4660 Å, and a WN7 emits $10^{35.1}$ ergs s^{-1} at 5810 Å and $10^{36.5}$ ergs s^{-1} at 4660 Å. Only one WC4 would be enough to explain simultaneously the luminosity detected in these two blends, since in the case of WN7, 25 stars are needed to explain the 5810 Å and these stars would emit $10^{37.9}$ ergs s^{-1} at 4660 Å, which represents much more energy than the emission we have detected.

The ratio of the luminosity of the 4660 Å bump to Hβ is 0.04, which implies a ratio of the number of W-R stars to the derived number of O7 stars of 0.03. Both numbers are compatible with the number predicted by the models of Cerviño & Mass-Hesse (1994) and Arnault, Kunth, & Schild (1989), following Maeder (1990).

4.6. *The Broad Low-Intensity Components*

Another important feature in the spectrum of NGC 2363 at both locations, knots A and B, is the broad low-intensity component under the Hα and [O III] λλ4959, 5007 lines. This component was previously detected by Roy et al. (1992) when they observed the object at P.A. = 90° across knot A. We thus confirm that this broad component extends about 500 pc, and since we observed the object in a position almost perpendicular to that of Roy et al. (1992), it is very likely that this emission has roughly spherical symmetry.

This broad component is very weak compared with the narrow component. The broad line flux was estimated by fitting a combination of narrow and broad Gaussians to the profile of [O III] λλ4959, 5007 and Hα. The Hα broad component flux is about 3% of the narrow one, except for the outer zones at P.A. = 187°, where it reaches 30%. The FWHM of the broad Gaussians is ~30 Å in Hα, corresponding to 1400 km s^{-1} (see Table 7); in the outer zones at P.A. = 187°, the FWHM are larger, ~2800 km s^{-1}.

The broad component of [O III] is similar to the Hα one, except for the outer zones at P.A. = 187°, where the [O III] component is more conspicuous than the Hα component. In this case, the FWHM is larger than 3500 km s^{-1}; however, in these locations the signal-to-noise ratio is low and the error in the determination of the FWHM is at least 25%.

The values of FWHM, the ratio of the broad to narrow component fluxes, and the ratio [O III]/Hα for the broad component are shown in Table 7. The latter ratio is quite similar to the ratio [O III]/Hα for the narrow component, assuming that the reddening for the broad component is equal to that for the narrow component.

Figure 15 shows some of the best fits of narrow and broad Gaussians to the Hα and [O III] lines.

5. DISCUSSION

5.1. *The Mass of the Star Cluster and of the Ionized Gas*

An ultraviolet input flux of 1.52×10^{52} photons s^{-1} is necessary to produce the measured Hα luminosity of NGC 2363. This photon luminosity is equivalent to 176 O4 V stars. We can make an estimate of the mass of the stellar cluster from the total number of ionizing photons by using evolutionary synthesis models.

Star cluster models based on evolutionary tracks by Fogotto et al. (1994) and the stellar atmosphere models by Kurucz (1992) have been computed by García-Vargas, Bressan, & Díaz (1994) for different metallicities down to 1/50 of solar. For a metallicity of 0.2 solar and a standard IMF with slope, upper mass limit, and lower mass limit of 2.35, 120 $M_\odot$, and 0.8 $M_\odot$, respectively, the mean number of ionizing photons per solar

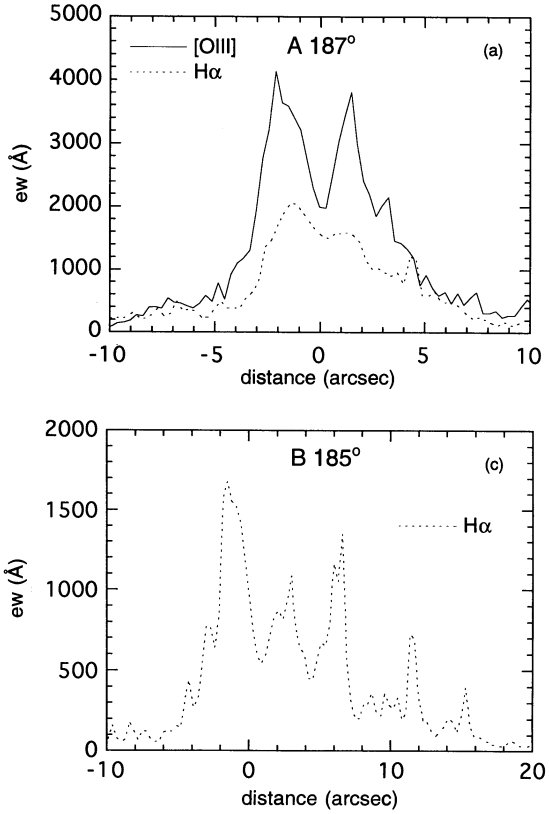

FIG. 11.—As in Fig. 8, for the equivalent width of the lines [O III] λ5007 and Hα. These profiles have been obtained dividing the emission line profile by a nearby continuum window profile.

mass of the clusters with age between 3 and 5 Myr is 4.5×10^{46} photons s^{-1} $M_{\odot}^{-1}$. Therefore, if the nebula is ionization bounded, for this Hα luminosity of 1.4×10^{40} ergs s^{-1}, a lower limit for the stellar cluster mass is about 3.4×10^5 $M_{\odot}$.[9]

[9] This result is fairly insensitive to the exact value of the metallicity; in particular, a change in metallicity from 0.12 to 0.24, as implied by the temperature fluctuations discussed in § 5.4, would not alter this value of the mass.

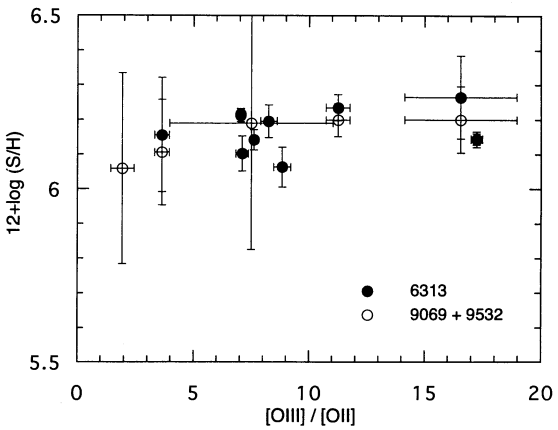

FIG. 12.—12 + log (S/H) vs. the excitation ratio [O III] λ5007/[O II] λ3727. The lack of correlation between sulfur abundance and excitation indicates the correctness of the S ICF used.

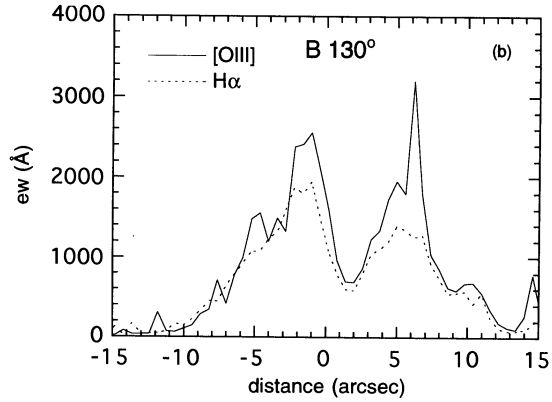

Following Osterbrock (1989), the mass of ionized gas is given by

$$M_{\mathrm{H}^+} = m_p \int_0^{R_S} \phi N_p \, dV = m_p \int_0^{R_S} \phi \frac{N_e}{1 + y^+} \, dV ,$$

where m_p and N_p are the proton mass and density, ϕ the volume filling factor, R_S the Strömgren radius, V the volume, N_e the electron density, and $y^+ = \mathrm{He}^+/\mathrm{H}^+$.

And the total ionized gas is given by

$$M_{\mathrm{H}^+ + \mathrm{He}^+} \sim m_p \phi N_e \frac{1 + 4y^+}{1 + y^+} V .$$

Using the weighted mean value obtained in § 4.3, $N_e = 190$ cm^{-3}, and the size and filling factor from § 3, $R_S = 250$ pc and $\phi = 0.008$, then a lower limit for the mass of ionized gas is $M_{\mathrm{H}^+ + \mathrm{He}^+} = 3 \times 10^5$ $M_{\odot}$, which is similar to the total mass of the stellar cluster.

5.2. *The Broad Component*

Our data confirm the existence of a broad low-intensity component in [O III] and Hα, as previously reported by Roy et al. (1992). This type of broad emission has been detected in other objects. Skillman & Kennicutt (1993), for example, have attributed the broad component in IZw18 to embedded supernova remnants. Castañeda, Vilchez, & Copetti (1990) have reported 300 km s^{-1} broad Hα emission in NGC 5471C, which

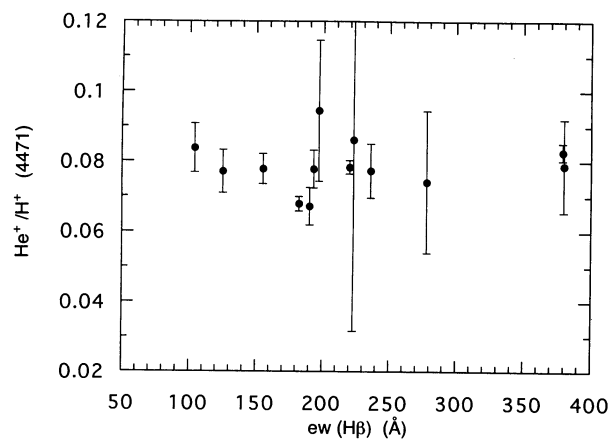

FIG. 13.—Ionic abundance of He^+ calculated with the line λ4471, $He^+(\lambda4471)/H^+$, vs. the equivalent width of Hβ, EW(Hβ). The lack of correlation indicates that He I λ4471 is not affected by underlying stellar absorption and shows the robust value of the He abundance.

TABLE 3A

REDDENING-CORRECTED FLUXES FOR KNOT A

Line	A1	A2	A3	A4
[O II] 3727	2.0 ± 0.4	0.432 ± 0.005	0.8 ± 0.4	1.0 ± 0.8
H12 3751	...	0.031 ± 0.002	...	...
H11 3770	...	0.031 ± 0.002	...	...
H10 3798	...	0.042 ± 0.003	...	...
He I 3820	...	0.007 ± 0.001	...	...
H9 + He II 3835	...	0.059 ± 0.005	...	...
[Ne III] 3868	0.30 ± 0.09	0.520 ± 0.007	0.5 ± 0.3	0.4 ± 0.5
H8 + He I 3888	0.19 ± 0.07	0.166 ± 0.001	0.24 ± 0.06	...
[Ne III] + Hε	0.15 ± 0.07	0.282 ± 0.002	0.4 ± 0.1	0.3 ± 0.4
He I 4009	...	0.002	...	...
He I 4026	...	0.015 ± 0.001	...	...
[S II] 4068, 76	...	0.005 ± 0.001	...	...
Hδ	0.23 ± 0.08	0.243 ± 0.002	0.21 ± 0.09	0.2 ± 0.2
He I 4121	...	0.002	...	...
He I 4142	...	0.003 ± 0.001	...	...
Hγ	0.5 ± 0.1	0.487 ± 0.004	0.5 ± 0.2	0.5 ± 0.4
[O III] 4363	0.09 ± 0.04	0.165 ± 0.004	0.13 ± 0.07	...
He I 4388	...	0.005 ± 0.001	...	...
He I 4471	...	0.038 ± 0.001	...	...
He II 4686	...	0.004 ± 0.001	...	...
[Ar IV] + He 4712	...	0.030 ± 0.001	...	...
[Ar IV] 4741	...	0.020 ± 0.001	...	...
Hβ	1 ± 0.2	1 ± 0.007	1 ± 0.37	1 ± 0.18
He I 4922	...	0.009 ± 0.001	± 0.42	...
[O III] 4959	1.3 ± 0.3	2.48 ± 0.02	2.03 ± 0.42	2.0 ± 0.35
[O III] 5007	3.9 ± 0.7	7.46 ± 0.06	6.14 ± 0.97	6 ± 1
[S III] 6312	0.01 ± 0.03	0.01 ± 0.001	...	...
Hα	2.8 ± 0.7	2.84 ± 0.02	2.6 ± 0.9	2.9 ± 0.4
[N II] 6584	0.08 ± 0.02	0.034 ± 0.001	0.05 ± 0.01	...
He I 6678	0.019 ± 0.006	0.029 ± 0.001	...	...
[S II] 6717	0.19 ± 0.04	0.038 ± 0.001	0.09 ± 0.02	0.15 ± 0.04
[S II] 6731	0.11 ± 0.02	0.029 ± 0.001	0.06 ± 0.01	0.1 ± 0.03
He I 7065	...	0.035 ± 0.001	...	...
[Ar III] 7135	0.06	0.053 ± 0.001	0.07 ± 0.02	...
He I 7281	...	0.005 ± 0.001	...	...
[O II] 7320	...	0.008 ± 0.001	...	...
[O II] 7330	...	0.007 ± 0.001	...	...
Pa 17 8467	...	0.003 ± 0.001	...	...
Pa 16 8502	...	0.005 ± 0.001	...	...
Pa 15 8545	...	0.006 ± 0.001	...	...
Pa 14 8598	...	0.007 ± 0.001	...	...
Pa 13 8665	...	0.008 ± 0.001	...	...
Pa 12 8750	...	0.011 ± 0.001	...	...
Pa 11 8863	...	0.014 ± 0.001	...	...
Pa 10 9014	...	0.018 ± 0.001	...	...
[S III] 9069	0.11 ± 0.05	0.083 ± 0.002	0.11 ± 0.03	0.2 ± 0.2
Pa 9 9229	...	0.027 ± 0.001	...	...
[S III] 9532	0.3 ± 0.2	0.23 ± 0.01	0.4 ± 0.3	0.4 ± 0.4
Pa 8 9546	...	0.034 ± 0.001	...	...
EW (Hβ)	81	379	191	140
log I(Hβ)	−14.21	−12.34	−14.37	−14.34

they attribute to stellar winds. Also, Sargent & Filippenko (1991) have detected Hα emission of full width at zero intensity of 2900 km s^{-1} in the knot 1 of the irregular galaxy NGC 4214, which they suggest is produced by WN8 stars, consistent with the W-R emission at 4660 Å they detected.

Roy et al. (1992) explore four mechanisms for the line broadening in NGC 2363: large velocities associated with stellar winds, supernova remnants, diffuse emission from the electron scattering, and the blowout of a superbubble. They argue that the latter mechanism is the only one capable of accelerating interstellar gas over 500 pc, but that the physical properties of the observed expanding bubble and the high inclination, 65°, of the galaxy appear to be incompatible with this mechanism. So they conclude that even though the broad emission is clearly attributed to very high velocity gas, its origin is unknown.

Let us consider again the possible mechanisms with the parameter values that we have obtained. We confirm that the broad component is ~500 pc in extension, also in the direction perpendicular to Roy's position angle, so that, to a good approximation, one can assume it presents spherical symmetry. The weighted mean FWHM for Hα is 29 Å. Assuming that the density of gas emitting in the broad component is equal to that of the narrow line gas, with an intensity ratio to the narrow component of 2.6%, and using the gas mass estimate from the previous section, we obtain a mass for the high-velocity gas of 6420 $M_\odot$ and a kinetic energy of 2.7 × 10^{52} ergs (assuming the gas is moving with a velocity equal to FWHM/

TABLE 3B

REDDENING-CORRECTED FLUXES FOR KNOT B (P.A. = 185°)

Line	WR 185	D1	D2	D3	D4	D5
[O II] 3727	0.71 ± 0.03	2.3 ± 0.4	0.84 ± 0.03	0.77 ± 0.03	0.9 ± 0.2	1.7 ± 0.7
H12 3751	0.015 ± 0.004	...	0.034 ± 0.004	0.020 ± 0.004	...	...
H11 3770	0.015 ± 0.004	...	0.034 ± 0.004	0.026 ± 0.004	...	...
H10 3798	0.023 ± 0.004	...	0.036 ± 0.004	0.029 ± 0.004	...	...
He I 3821	0.009	...	0.010 ± 0.002	0.03 ± 0.01	...	...
H9 + He II 3835	0.050 ± 0.006	...	0.069 ± 0.005	0.059 ± 0.006	0.12 ± 0.04	...
[Ne III] 3868	0.51 ± 0.02	0.41 ± 0.13	0.48 ± 0.02	0.48 ± 0.02	0.5 ± 0.12	0.49 ± 0.09
H8 + He I 3888	0.18 ± 0.01	0.23 ± 0.04	0.18 ± 0.01	0.18 ± 0.01	0.24 ± 0.05	0.33 ± 0.06
Ne III] + H I 3968	0.25 ± 0.01	0.24 ± 0.04	0.27 ± 0.01	0.25 ± 0.01	0.33 ± 0.06	0.26 ± 0.05
[S II] 4068, 76	...	...	0.01 ± 0.002	0.01 ± 0.002	...	...
Hδ 4101	0.25 ± 0.01	0.28 ± 0.05	0.25 ± 0.01	0.24 ± 0.01	0.37 ± 0.07	0.22 ± 0.04
Hγ 4340	0.47 ± 0.02	0.43 ± 0.07	0.48 ± 0.01	0.47 ± 0.02	0.51 ± 0.09	0.46 ± 0.08
[O III] 4363	0.148 ± 0.008	...	0.126 ± 0.007	0.123 ± 0.006	0.11 ± 0.04	...
He I 4471	0.038 ± 0.003	...	0.036 ± 0.002	0.036 ± 0.003	0.05 ± 0.03	...
He II 4686	0.034 ± 0.004	...	0.014 ± 0.002	0.032 ± 0.009	...	...
[Ar IV] + He 4712	0.016 ± 0.003	...	0.013 ± 0.002	0.018 ± 0.003	...	...
[Ar IV] 4741	0.011 ± 0.003	...	0.011 ± 0.002	0.008 ± 0.002	...	...
Hβ	1 ± 0.02	1 ± 0.2	1 ± 0.02	1 ± 0.02	1 ± 0.07	1 ± 0.2
He I 4921	...	...	0.009 ± 0.002	0.010 ± 0.002	...	...
[O III] 4959	2.12 ± 0.04	1.3 ± 0.3	1.99 ± 0.04	2.13 ± 0.05	2.2 ± 0.2	1.6 ± 0.4
[O III] 5007	6.3 ± 0.1	3.9 ± 0.7	5.8 ± 0.1	6.36 ± 0.13	6.6 ± 0.5	5 ± 1
He I 5012	0.032 ± 0.003	...	0.033 ± 0.003	0.027 ± 0.003	...	...
He I 5876	0.096 ± 0.004	0.11 ± 0.02	0.098 ± 0.004	0.097 ± 0.004	0.10 ± 0.02	...
[O I] 6300	0.016 ± 0.002	0.20 ± 0.03	0.022 ± 0.002	0.019 ± 0.002	0.05 ± 0.05	0.25 ± 0.04
[S III] 6312	0.014 ± 0.001	...	0.014 ± 0.001	0.016 ± 0.001	...	...
[O I] 6363	0.005 ± 0.001	0.10 ± 0.02	0.008 ± 0.001	0.006 ± 0.001	0.03 ± 0.02	0.9 ± 0.2
Hα	2.83 ± 0.05	2.5 ± 0.4	2.73 ± 0.05	2.81 ± 0.05	2.75 ± 0.25	2.7 ± 0.5
[N II] 6584	0.024 ± 0.001	0.06 ± 0.02	0.029 ± 0.001	0.024 ± 0.001	0.02 ± 0.01	0.05 ± 0.02
He I 6678	0.029 ± 0.001	0.04 ± 0.02	0.027 ± 0.002	0.027 ± 0.002	0.03 ± 0.01	...
[S II] 6717	0.055 ± 0.002	0.22 ± 0.05	0.075 ± 0.002	0.060 ± 0.002	0.07 ± 0.01	0.17 ± 0.05
[S II] 6731	0.042 ± 0.002	0.14 ± 0.04	0.053 ± 0.002	0.045 ± 0.002	0.06 ± 0.01	0.09 ± 0.03
EW (Hβ)	104	112	193	125	223	88
log I(Hβ)	−13.30	−13.99	−12.98	−13.15	−13.72	−14.12

TABLE 3C

REDDENING-CORRECTED FLUXES FOR KNOT B (P.A. = 130°)

Line	B1	B2	B3	B4	B5	WR 130
[O II] 3727	1.5 ± 0.1	0.89 ± 0.014	0.6 ± 0.03	0.42 ± 0.06	0.50 ± 0.09	0.84 ± 0.01
H12 3751	0.03 ± 0.01	0.028 ± 0.002	0.020 ± 0.003	0.012 ± 0.008	...	0.027 ± 0.002
H11 3770	0.019 ± 0.007	0.032 ± 0.002	0.028 ± 0.004	...	...	0.029 ± 0.002
H10 3798	0.03 ± 0.01	0.043 ± 0.002	0.028 ± 0.004	0.04 ± 0.01	0.03 ± 0.02	0.043 ± 0.002
He I 3821	...	0.008 ± 0.001	0.012 ± 0.01	...	...	0.008 ± 0.001
H9 + He II	0.07 ± 0.01	0.069 ± 0.002	0.053 ± 0.005	0.05 ± 0.01	0.05 ± 0.03	0.068 ± 0.003
[Ne III] 3868	0.43 ± 0.04	0.48 ± 0.01	0.47 ± 0.02	0.41 ± 0.05	0.6 ± 0.01	0.51 ± 0.01
H8 + He I 3888	0.2 ± 0.02	0.193 ± 0.004	0.177 ± 0.009	0.14 ± 0.02	0.198 ± 0.05	0.2 ± 0.005
[Ne III] + H I 3968	0.26 ± 0.03	0.290 ± 0.005	0.25 ± 0.01	0.24 ± 0.03	0.31 ± 0.06	0.302 ± 0.006
He I 4026	...	0.015 ± 0.001	0.010 ± 0.002	...	...	0.012 ± 0.001
[S II] 4068, 76	0.015 ± 0.005	0.011 ± 0.001	...	...	...	0.010 ± 0.001
Hδ 4101	0.25 ± 0.03	0.259 ± 0.005	0.23 ± 0.01	0.23 ± 0.03	0.20 ± 0.04	0.260 ± 0.005
Hγ 4340	0.50 ± 0.04	0.492 ± 0.007	0.46 ± 0.01	0.46 ± 0.04	0.46 ± 0.06	0.494 ± 0.007
[O III] 4363	0.11 ± 0.02	0.125 ± 0.002	0.13 ± 0.005	0.14 ± 0.02	0.13 ± 0.02	0.133 ± 0.004
He I 4471	0.04 ± 0.01	0.036 ± 0.001	0.312 ± 0.002	0.034 ± 0.009	...	0.036 ± 0.002
He II 4686	...	0.022 ± 0.001	0.026 ± 0.005	0.02 ± 0.007	...	0.031 ± 0.001
[Ar IV] + He I 4712	...	0.017 ± 0.001	0.020 ± 0.003	0.024 ± 0.008	...	0.019 ± 0.001
[Ar IV] 4741	...	0.010 ± 0.003	0.010 ± 0.002	...	...	0.013 ± 0.001
Hβ	1 ± 0.06	1 ± 0.006	1 ± 0.02	1 ± 0.06	1 ± 0.04	1 ± 0.007
He I 4921	...	0.009 ± 0.009	0.006 ± 0.002	0.012 ± 0.006	...	0.007 ± 0.001
[O III] 4959	1.8 ± 0.1	2.11 ± 0.02	2.25 ± 0.04	2.3 ± 0.1	2.3 ± 0.2	2.12 ± 0.02
[O III] 6007	5.3 ± 0.3	6.29 ± 0.06	6.8 ± 0.1	6.9 ± 0.4	6.8 ± 0.4	6.37 ± 0.05
He I 5012	0.07 ± 0.01	0.017 ± 0.001	0.052 ± 0.004	...	0.07 ± 0.02	0.026 ± 0.001
He I 5876	0.11 ± 0.02	0.098 ± 0.006	0.107 ± 0.004	0.10 ± 0.01	0.09 ± 0.02	0.093 ± 0.002
[O I] 6300	0.15 ± 0.02	0.018 ± 0.001	0.017 ± 0.001	0.017 ± 0.004	0.11 ± 0.02	0.016 ± 0.001
[S III] 6312	0.017 ± 0.006	0.017 ± 0.001	0.015 ± 0.001	0.016 ± 0.003	...	0.016 ± 0.001
[O I] 6363	0.031 ± 0.008	0.007	0.007 ± 0.001	0.006 ± 0.002	0.08 ± 0.02	0.005
Hα	2.8 ± 0.1	2.71 ± 0.03	3.14 ± 0.05	3.1 ± 0.2	2.8 ± 0.2	2.62 ± 0.02
[N II] 6584	0.053 ± 0.005	0.030 ± 0.001	0.022 ± 0.002	0.018 ± 0.003	0.02 ± 0.006	0.024 ± 0.001
He I 6678	0.027 ± 0.004	0.027 ± 0.001	0.030 ± 0.001	0.029 ± 0.003	0.027 ± 0.005	0.026 ± 0.001
[S II] 6717	0.13 ± 0.01	0.072 ± 0.001	0.053 ± 0.002	0.044 ± 0.004	0.046 ± 0.007	0.055 ± 0.001
[S II] 6731	0.09 ± 0.01	0.054 ± 0.001	0.039 ± 0.002	0.034 ± 0.003	0.038 ± 0.006	0.043 ± 0.001
EW (Hβ)	197	220	190	278	70	155
log I(Hβ)	−13.90	−13.98	−13.57	14.06	−14.11	−13.26

TABLE 3D

REDDENING-CORRECTED FLUXES FOR KNOT B (P.A. = 130°)

Line	C1	C2	C3	C4	C5
[O II] 3727	1.2 ± 0.3	0.77 ± 0.01	0.59 ± 0.03	0.49 ± 0.05	0.48 ± 0.4
H12 3751	...	0.021 ± 0.001	0.016 ± 0.002	0.024 ± 0.008	...
H11 3770	...	0.023 ± 0.001	0.019 ± 0.003	0.021 ± 0.008	...
H10 3798	0.05 ± 0.01	0.037 ± 0.001	0.039 ± 0.004	0.04 ± 0.01	...
He I 3821	...	...	...	...	...
H9 + He II	0.030 ± 0.007	0.050 ± 0.002	0.047 ± 0.004	0.04 ± 0.01	...
[Ne III] 3868	0.4 ± 0.1	0.436 ± 0.007	0.49 ± 0.02	0.48 ± 0.05	0.43 ± 0.07
H8 + He I 3888	0.17 ± 0.04	0.155 ± 0.003	0.185 ± 0.009	0.17 ± 0.02	0.18 ± 0.04
[Ne III] + H I 3968	0.24 ± 0.05	0.250 ± 0.004	0.30 ± 0.01	0.29 ± 0.03	0.34 ± 0.06
He I 4027	...	0.010 ± 0.001	0.013 ± 0.002	...	...
[S II] 4068, 76	...	0.006 ± 0.001	...	...	...
Hδ 4101	0.25 ± 0.05	0.229 ± 0.004	0.26 ± 0.01	0.24 ± 0.03	0.22 ± 0.04
Hγ 4340	0.5 ± 0.1	0.48 ± 0.006	0.53 ± 0.02	0.5 ± 0.05	0.54 ± 0.08
[O III] 4363	0.09 ± 0.07	0.119 ± 0.002	0.136 ± 0.008	0.11 ± 0.01	0.11 ± 0.02
He I 4471	0.03 ± 0.03	0.031 ± 0.001	0.036 ± 0.004	0.037 ± 0.006	...
He II 4686	...	0.024 ± 0.002	0.025 ± 0.003	0.022 ± 0.007	...
[Ar IV] + He I 4712	...	0.016 ± 0.001	0.023 ± 0.003	0.024 ± 0.008	...
[Ar IV] 4741	...	0.010 ± 0.001	0.011 ± 0.002	0.015 ± 0.006	...
Hβ	1 ± 0.2	1 ± 0.009	1 ± 0.03	1 ± 0.06	1 ± 0.09
He I 4921	...	0.010 ± 0.001	0.011 ± 0.003	0.032 ± 0.009	...
[O III] 4959	1.7 ± 0.4	2.11 ± 0.02	2.2 ± 0.1	2.3 ± 0.2	2.3 ± 0.2
[O III] 5007	5 ± 1	6.29 ± 0.06	6.6 ± 0.2	6.9 ± 0.5	6.8 ± 0.6
Pa 16 8502	...	0.003 ± 0.001	...	...	...
Pa 15 8545	...	0.004 ± 0.001	...	...	...
Pa 14 8598	...	0.007 ± 0.001	...	...	...
Pa 13 8665	...	0.008 ± 0.001	...	...	...
Pa 12 8750	...	0.010 ± 0.001	...	...	...
Pa 11 8863	...	0.011 ± 0.001	...	...	...
Pa 10 9014	0.018 ± 0.004	0.02 ± 0.002	0.02 ± 0.009	0.02 ± 0.02	...
[S III] 9069	0.10 ± 0.04	0.11 ± 0.004	0.10 ± 0.02	0.09 ± 0.02	0.11 ± 0.03
Pa 9 9229	0.022 ± 0.005	0.03 ± 0.002	0.02 ± 0.01	0.02 ± 0.05	...
[S III] 9532	0.3 ± 0.3	0.36 ± 0.03	0.29 ± 0.09	0.3 ± 0.1	0.3 ± 0.2
Pa 8 9546	0.05 ± 0.01	0.03 ± 0.01	0.03 ± 0.03	0.03 ± 0.06	...
EW (Hβ)	...	182	236	380	56
log I(Hβ)	−13.91	−12.98	−13.73	−14.17	−14.19

TABLE 4

REDDENING, TEMPERATURES, AND DENSITIES

Spectrum	T [O III]	T [S III]	T [S II]	T [O II]	T [O II] St[a]	x	Ne	C(Hβ)
A1	1.62 ± 0.80	...	...	...	1.43 ± 0.56	...	...	0.19
A2	1.61 ± 0.04	1.71 ± 0.17	1.34 ± 0.33	1.45 ± 0.13	1.43 ± 0.03	0.019	235 ± 41	0.20
A3	1.59 ± 1.0	...	...	...	1.42 ± 0.71	0.004	50 ± 490	0.18
A4	...	...	...	...	...	0.001	...	0.18
A5	...	...	...	...	...	0.066	...	...
B1	1.55 ± 0.29	1.83 ± 2.50	1.20 ± 0.85	...	1.38 ± 0.20	0.013	159 ± 210	0.25
B2	1.52 ± 0.03	1.59 ± 0.20	1.54 ± 0.25	...	1.37 ± 0.02	0.013	163 ± 39	0.16
B3	1.50 ± 0.06	1.68 ± 0.70	...	...	1.35 ± 0.05	0.013	153 ± 80	0.20
B4	1.53 ± 0.21	1.83 ± 1.30	...	...	1.37 ± 0.15	0.017	214 ± 200	0.20
B5	1.50 ± 0.29	...	...	...	1.35 ± 0.21	0.027	331 ± 350	0.20
WR 130	1.57 ± 0.05	...	1.62 ± 0.33	...	1.40 ± 0.04	0.019	241 ± 52	0.16
C1	1.48 ± 1.30	...	...	...	1.33 ± 0.88	...	...	...
C2	1.49 ± 0.03	...	...	...	1.34 ± 0.02	...	...	...
C3	1.54 ± 0.11	...	...	...	1.38 ± 0.08	...	...	...
C4	1.37 ± 0.17	...	...	...	1.26 ± 0.12	...	...	...
C5	1.35 ± 0.28	...	...	...	1.24 ± 0.20	...	...	...
D1	...	...	...	...	...	...	...	0.30
D2	1.58 ± 0.09	...	1.55 ± 0.85	...	1.40 ± 0.07	0.007	93 ± 62	0.18
D3	1.51 ± 0.08	...	1.62 ± 0.87	...	1.36 ± 0.06	0.013	155 ± 88	0.18
D4	1.40 ± 0.51	...	...	...	1.28 ± 0.36	0.020	240 ± 410	0.24
D5	...	...	...	...	...	0.0	...	0.24
WR185	1.66 ± 0.11	...	...	...	1.46 ± 0.08	0.017	220 ± 100	0.18
A1 b2[b]	1.59 ± 0.49	...	...	...	1.41 ± 0.34	...	...	...
A2 b2[b]	1.59 ± 0.03	...	1.66 ± 0.11	...	1.41 ± 0.02	...	...	...
A3 b2[b]	1.71 ± 0.65	...	...	...	1.49 ± 0.45	...	...	...

NOTE.—Temperature is in units of 10^4 K, and density in units of cm^{-3}.

[a] St = as calculated with Stasińska 1982 formula $t(O^+) = 0.7t(O^{+2}) + 0.3$.

[b] These three spectra (marked b2) correspond to the two longest integration time frames taken in February, where the line [O III] λ5007 is saturated, and hence T_e([O III]) has been obtained from the ratio of λ4363/4 × λ4959.

TABLE 5A

IONIC ABUNDANCES

Spectrum	O^{+} [a]	O^{+2} [a]	O^{+}/N^{+} [b]	O^{+2}/Ne^{+2} [b]	S^{+} [a]	S^{+2} [a,c]	S^{+2} [a,d]	ICF S
A1	7.28 ± 0.94	7.55 ± 0.63	1.47 ± 0.42	0.78 ± 0.23	5.49 ± 0.53	...	5.82 ± 0.40	1.18
A2	6.63 ± 0.05	5.84 ± 0.03	1.51 ± 0.02	0.82 ± 0.01	4.86 ± 0.03	5.75 ± 0.05	5.75 ± 0.03	2.20
A3	6.91 ± 1.20	7.76 ± 0.82	1.32 ± 0.57	0.77 ± 0.34	5.18 ± 0.68	...	5.89 ± 0.58	1.66
B1	7.20 ± 0.35	7.73 ± 0.23	1.54 ± 0.16	0.75 ± 0.08	5.39 ± 0.20	5.91 ± 0.35	...	1.35
B2	7.00 ± 0.04	7.82 ± 0.03	1.59 ± 0.02	0.77 ± 0.01	5.16 ± 0.02	5.93 ± 0.04	...	1.64
B3	6.84 ± 0.08	7.86 ± 0.05	2.18 ± 0.08	0.81 ± 0.02	5.03 ± 0.05	5.90 ± 0.08	...	1.91
B4	6.67 ± 0.27	7.85 ± 0.18	1.48 ± 0.15	0.88 ± 0.07	4.94 ± 0.15	5.88 ± 0.25	...	2.18
B5	6.77 ± 0.38	7.87 ± 0.25	1.51 ± 0.22	0.73 ± 0.11	5.00 ± 0.21	...	...	2.00
WR 130	6.95 ± 0.07	7.79 ± 0.04	1.65 ± 0.03	0.75 ± 0.02	5.04 ± 0.04	5.85 ± 0.06	...	1.68
C1	7.18 ± 1.6	7.75 ± 1.1	...	0.74 ± 0.34	...	...	5.87 ± 0.64	1.38
C2	6.96 ± 0.04	7.84 ± 0.03	...	0.81 ± 0.01	...	...	5.95 ± 0.03	1.72
C3	6.81 ± 0.13	7.83 ± 0.09	...	0.78 ± 0.03	...	...	5.84 ± 0.11	1.91
C4	6.86 ± 0.23	7.98 ± 0.16	...	0.79 ± 0.07	...	...	5.87 ± 0.17	2.03
C5	6.88 ± 0.39	8.01 ± 0.27	...	0.86 ± 0.11	...	...	5.99 ± 0.27	2.06
D2	6.93 ± 0.11	7.76 ± 0.08	1.55 ± 0.06	0.76 ± 0.03	5.14 ± 0.06	5.80 ± 0.11	...	1.65
D3	6.95 ± 0.10	7.83 ± 0.07	1.61 ± 0.05	0.77 ± 0.03	5.08 ± 0.06	5.89 ± 0.10	...	1.73
D4	7.09 ± 0.67	7.93 ± 0.46	1.72 ± 0.33	0.75 ± 0.17	5.23 ± 0.38	...	...	1.64
WR 185	6.81 ± 0.13	7.73 ± 0.09	1.56 ± 0.06	0.76 ± 0.03	5.00 ± 0.07	5.74 ± 0.12	...	1.78
A1 b2	7.35 ± 0.58	7.58 ± 0.39	...	0.67 ± 0.14	...	...	...	...
A2 b2	6.61 ± 0.04	7.86 ± 0.03	...	0.86 ± 0.01	...	...	...	...
A3 b2	6.84 ± 0.74	7.65 ± 0.49	...	0.75 ± 0.20	...	...	...	...

[a] These columns are in fact $12 + \log X$.
[b] These columns are $\log X$.
[c] These columns are $12 + \log (S^{+2})$, computed from the intensity of the line λ6312.
[d] The columns are $12 + \log (S^{+2})$, computed from the intensity of the lines [S III] $\lambda\lambda$9069, 9532.

$2 = 660$ km s^{-1}). This value of the kinetic energy is some 25 times smaller than the one calculated by Roy et al. (1992),[10] Following these authors, 100 massive stars would be needed to produce this much kinetic energy from their winds. This number is a fourth of the number deduced by Roy et al., and it is compatible with the mass of the stellar cluster which we deduce in § 5.1. The problem of the huge extension of the broad component remains unsolved.

[10] Note that our mean velocity is smaller than Roy's because the width decreases inwards, and while we use a weighted mean value, Roy et al. use a value measured in the outer parts, where the velocity is larger.

5.3. *The Hardness of the Ionizing Spectrum*

It is well known that giant H II regions are excited by a cluster of massive stars. In a typical giant region, the gas is ionized by the equivalent of less than a hundred O5 V stars. The emergent spectrum from such cluster is characterized by

TABLE 5B

He ABUNDANCES

Spectrum	He^{+} [a]	He^{+} [b]	He^{+} [c]	He^{+2}
A1	...	...	0.053 ± 0.019	...
A2	0.083 ± 0.003	...	0.080 ± 0.002	0.0004 ± 0.00004
A3	...	...	...	...
B1	0.094 ± 0.020	0.088 ± 0.014	0.077 ± 0.012	...
B2	0.078 ± 0.002	0.080 ± 0.005	0.072 ± 0.002	0.0024 ± 0.0001
B3	0.067 ± 0.005	0.087 ± 0.003	0.080 ± 0.004	0.0028 ± 0.0006
B4	0.074 ± 0.020	0.084 ± 0.011	0.079 ± 0.008	0.0025 ± 0.0008
B5	...	0.071 ± 0.013	0.073 ± 0.015	...
WR 130	0.078 ± 0.004	0.076 ± 0.002	0.075 ± 0.002	0.0034 ± 0.0001
C1	0.059 ± 0.056	...	...	...
C2	0.068 ± 0.002	...	...	0.0027 ± 0.0003
C3	0.077 ± 0.008	...	...	0.0027 ± 0.0003
C4	0.079 ± 0.013	...	...	0.0025 ± 0.0007
D2	0.078 ± 0.005	0.080 ± 0.004	0.073 ± 0.005	0.0015 ± 0.0002
D3	0.077 ± 0.006	0.078 ± 0.003	0.071 ± 0.005	0.0035 ± 0.001
D4	0.086 ± 0.054	0.082 ± 0.018	0.067 ± 0.025	...
WR 185	0.084 ± 0.007	0.079 ± 0.003	0.080 ± 0.004	0.0037 ± 0.0004
A2 b2	0.084 ± 0.001	...	...	0.0004 ± 0.00001

[a] He^{+}/H^{+} has been computed from the intensity of the line λ4471.
[b] He^{+}/H^{+} has been computed from the intensity of the line He I λ5876.
[c] He^{+}/H^{+} has been computed from the intensity of the line He I λ6678.

TABLE 5C

TOTAL ABUNDANCES

Spectrum	O/H[a]	Ne/H[a]	N/H[a]	S 6312[a]	S 9059[a]	He/H[b]	He/H 6678
A1	7.74 ± 0.47	6.77 ± 0.67	6.27 ± 0.63	...	6.06 ± 0.27	0.05 ± 0.02	0.05 ± 0.02
A2	7.86 ± 0.02	7.02 ± 0.04	6.35 ± 0.03	6.14 ± 0.02	6.14 ± 0.02	0.081 ± 0.001	0.081 ± 0.002
A3	7.82 ± 0.61	6.99 ± 0.88	6.50 ± 0.83	...	6.19 ± 0.36	...	...
B1	7.84 ± 0.17	6.98 ± 0.25	6.30 ± 0.23	6.16 ± 0.17	6.11 ± 0.15	0.084 ± 0.008	0.08 ± 0.01
B2	7.89 ± 0.02	7.05 ± 0.03	6.31 ± 0.03	6.21 ± 0.02	6.22 ± 0.02	0.078 ± 0.001	0.075 ± 0.002
B3	7.92 ± 0.04	7.06 ± 0.06	5.73 ± 0.09	6.23 ± 0.04	6.20 ± 0.05	0.084 ± 0.002	0.083 ± 0.004
B4	7.89 ± 0.13	6.97 ± 0.19	6.41 ± 0.20	6.26 ± 0.12	6.20 ± 0.10	0.083 ± 0.006	0.082 ± 0.008
B5	7.90 ± 0.19	7.14 ± 0.27	6.39 ± 0.28	...	...	0.07 ± 0.01	0.07 ± 0.02
WR 130	7.87 ± 0.03	7.04 ± 0.05	6.22 ± 0.05	6.14 ± 0.03	...	0.079 ± 0.001	0.078 ± 0.002
C1	7.85 ± 0.79	7.01 ± 1.10	...	...	...	0.06 ± 0.06	...
C2	7.91 ± 0.02	7.03 ± 0.03	...	...	...	0.070 ± 0.002	...
C3	7.88 ± 0.07	7.04 ± 0.10	...	...	...	0.080 ± 0.008	...
C4	8.00 ± 0.12	7.18 ± 0.17	...	...	...	0.08 ± 0.01	...
C5	8.04 ± 0.19	7.16 ± 0.29	...	...	...	...	...
D2	7.83 ± 0.06	7.00 ± 0.08	6.28 ± 0.08	6.10 ± 0.05	...	0.079 ± 0.003	0.074 ± 0.005
D3	7.90 ± 0.05	7.06 ± 0.08	6.29 ± 0.07	6.19 ± 0.05	...	0.080 ± 0.003	0.074 ± 0.005
D4	7.99 ± 0.34	7.17 ± 0.49	6.27 ± 0.47	...	...	0.077 ± 0.014	0.067 ± 0.025
WR 185	7.80 ± 0.06	6.97 ± 0.09	6.24 ± 0.09	6.06 ± 0.06	...	0.084 ± 0.002	0.084 ± 0.004
A1 b2	7.78 ± 0.29	6.90 ± 0.42	...	...	...	...	...
A2 b2	7.89 ± 0.02	7.00 ± 0.03	...	...	...	0.08 ± 0.001	...
A3 b2	7.71 ± 0.36	6.89 ± 0.53	...	...	...	...	...
Mean	7.89 ± 0.009	7.03 ± 0.01	6.28 ± 0.02	6.18 ± 0.01	6.18 ± 0.01	0.080 ± 0.0005	0.079 ± 0.001
Knot A	7.86 ± 0.020	7.02 ± 0.04	6.35 ± 0.03	6.14 ± 0.02	6.14 ± 0.02	0.081 ± 0.001	0.080 ± 0.002
Knot B	7.89 ± 0.009	7.03 ± 0.01	6.25 ± 0.02	6.18 ± 0.01	6.21 ± 0.02	0.080 ± 0.0006	0.077 ± 0.001

[a] These columns are in fact 12 + log X.

[b] This is the mean value using the two or three emission lines as available.

high excitation lines, such as [O III] λλ5007, 4363; however, very high excitation lines, such as [Ne V] λ3425 and He II λ4686, have not been detected in most of them. In the last few years, it has been found that some giant H II regions in the Local Group show He II λ4686 in emission. Some of these regions are IC 1613 and N76 in the Small Magellanic Cloud (SMC), and they present a ratio L(He II 4686)/L(Hβ) ~ 0.05 (Garnett 1991). This line has been detected also in dwarf emission line galaxies (Campbell, Terlevich, & Melnick 1986). Bergeron (1977) has suggested that this emission arises in the atmospheres of Of stars; however, because in these H II regions the line N III λ4640 is not present, Conti (1991) has suggested that the He II line could be excited by W-R stars.

In NGC 2363, we have observed in both knots the narrow line He II λ4686 in emission. The line is extended in both positions (cf. Figs. 4 and 5), especially in knot B, where we have detected the W-R bump, the narrow He II line is extended 12″, and it is brighter than in knot A. For knot A, L(He II)/L(Hβ) = 0.005, and for knot B, it is in the range 0.015–0.035; these values are similar to the average ratio of 0.02 found in dwarf emission line galaxies (Campbell et al. 1986).

The ratios indicate that the ionizing spectrum is very hard and more so in knot B than in A, and even the total He II luminosity is a factor of 2 larger in knot B than in A. This is in contrast with the fact that the ratios [O III]/Hβ and [O III]/[O II] are smaller in knot B than in knot A. Probably, the presence of some W-R stars in a cluster does not much change the number of Lyman ionizing photons, but increase considerably the number of photons with energy higher than 54 eV, thus significantly raising the ratio He II λ4686/Hβ while barely changing [O III]/Hβ and [O III]/[O II].

Thus NGC 2363 is a good example where the W-R bumps at 4660 Å and at 5810 Å, attributed to a WC star, and a narrow emission He II λ4686 line are present.

TABLE 6

THE W-R EMISSION

Blend	Flux$^{\rm blend\,a}$ (ergs s^{-1} cm^{-2})	Flux$^{\rm cont\,b}$ (ergs s^{-1} cm^{-2})	EW (Å)	log $L^{\rm blend}$ (ergs s^{-1})
Blend λ4660 (P.A. = 130°, Feb)	5.04	3.39	14.9	36.9
Blend λ4660 (P.A. = 130°, Oct)	3.03	2.59	11.7	36.7
Blend λ4660 (P.A. = 185°, Oct)	4.20	3.52	11.9	36.8
Blend λ5800 (P.A. = 130°, Oct)	2.07	1.51	13.7	36.5
Blend λ5800 (P.A. = 185°, Oct)	1.91	1.81	10.5	36.5

[a] Flux in units of 10^{-15}.

[b] Flux in units of 10^{-16}.

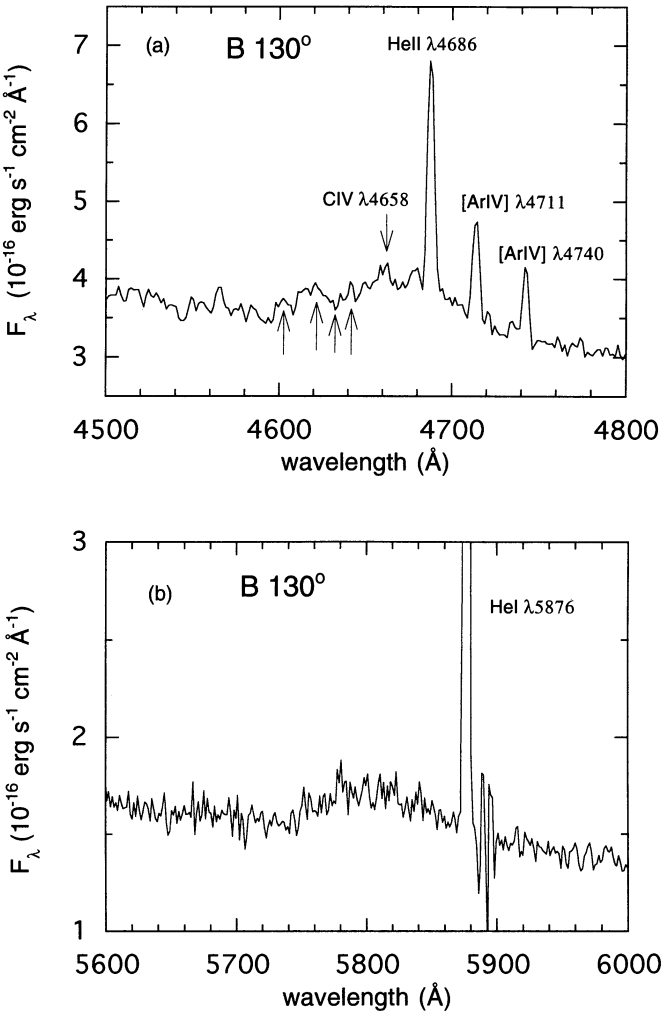

FIG. 14.—Merged spectrum of knot B showing an enlargement of the W-R features at (*a*) 4660 Å and (*b*) 5810 Å. The arrows indicate the wavelength position of the stellar lines N V λλ4604, 4620 and N III λλ4634, 4652.

5.4. *Temperature Fluctuations inside the Region and Their Effect in the Determination of the Chemical Abundances*

There are several methods to calculate the electron temperature of an H II region (see, e.g., Aller 1984; Osterbrock 1989). The most common imply using the intensity ratio of auroral to nebular collisionally excited lines, from ions like O^{+2}, S^{+2}, S^{+}, and O^{+}; this is the method we have used in § 4.3. A second method involves radio continuum measurements, using ratios of bound-bound to free-free transitions of hydrogen. A third method, which we can apply to our optical data, uses ratios of the bound-free (series limits) to bound-bound recombination transitions of hydrogen and helium. In this case we can use the ratio of the Balmer or Paschen discontinuity to the intensity of Hβ to calculate the electron temperature, since the emission in the continuum depends on the width of the free-electron velocity distribution function, hence on T_e.

The Paschen discontinuity in emission in knot A (spectrum A2, Fig. 16) and in knot B (spectrum C2) implies $(0.75 \pm 0.19) \times 10^{-16}$ and $(0.23 \pm 0.11) \times 10^{-16}$ ergs s^{-1} cm^{-2} Å^{-1}, respectively. The emission was measured as the difference between the continuum levels obtained by fitting a line to the continuum regions at $\lambda < 8200$ Å and at $\lambda > 8600$ Å, that were extrapolated to 8200 Å. The error in the jump has been calculated to be $2^{1/2}$ times one sigma of the continuum. Several independent measurements have been done, with errors lower than 0.05 and 0.03×10^{-16} ergs s^{-1} cm^{-2} Å^{-1} for knots A and B, respectively.

Given the low reddening obtained (cf. Table 4), it is sound to assume that these values reflect the intrinsic Paschen discontinuity, without contamination by dust-scattered radiation. Unfortunately, our observed wavelength range starts just longwards of the Balmer limit.

To obtain the electron temperature we have computed theoretical nebular Paschen continuum emission normalized to the intensity of Hβ in the following way,

$$\frac{\Delta Pa}{\mathrm{H}\beta} = 2.445 \times 10^{-15}\left[\frac{\Delta\gamma_\nu(\mathrm{H}^0, T)}{\alpha^{\mathrm{eff}}_{\mathrm{H}\beta}(\mathrm{H}^0, T)} + \frac{\mathrm{He}^+}{\mathrm{H}^+}\frac{\Delta\gamma_\nu(\mathrm{He}^0, T)}{\alpha^{\mathrm{eff}}_{\mathrm{H}\beta}(\mathrm{H}^0, T)} + \frac{\mathrm{He}^{++}}{\mathrm{H}^+}\frac{\Delta\gamma_\nu(\mathrm{He}^+, T)}{\alpha^{\mathrm{eff}}_{\mathrm{H}\beta}(\mathrm{H}^0, T)}\right](\mathrm{Hz}^{-1}),$$

where the values of $\Delta\gamma_\nu$ have been obtained from the tables of Brown & Mathews (1970). These authors include in their cal-

TABLE 7

BROAD COMPONENT WIDTH, BROAD-TO-NARROW INTENSITY RATIOS, AND EXCITATION RATIO FOR THE BROAD AND NARROW COMPONENTS

Spectrum	FWHM Hα (Å)	$\mathrm{H}\alpha^b/\mathrm{H}\alpha^n$	FWHM [O III] (Å)	$[\mathrm{O\ III}]^b/[\mathrm{O\ III}]^n$	$([\mathrm{O\ III}]/\mathrm{H}\alpha)^b$	$([\mathrm{O\ III}]/\mathrm{H}\alpha)^n$
A1	58 ± 8	0.34	94 ± 11	0.60	2.1	1.3
A2	30 ± 2	0.03	29 ± 1	0.03	2.3	2.3
A3	71 ± 18	0.25	57 ± 15	0.21	1.7	2.0
B1	42 ± 8	0.06	30 ± 5	0.45	1.2	1.3
B2	25 ± 2	0.02	20 ± 2	0.02	1.5	2.1
B3	26 ± 3	0.03	22 ± 2	0.02	1.5	1.9
B4	33 ± 5	0.04	25 ± 4	0.03	1.6	2.0
B5	60 ± 23	0.13	...	...	...	...
D1	30 ± 12	0.11	...	...	...	...
D2	28 ± 3	0.02	20 ± 3	0.02	1.6	1.9
D3	31 ± 4	0.02	22 ± 3	0.02	1.5	2.0

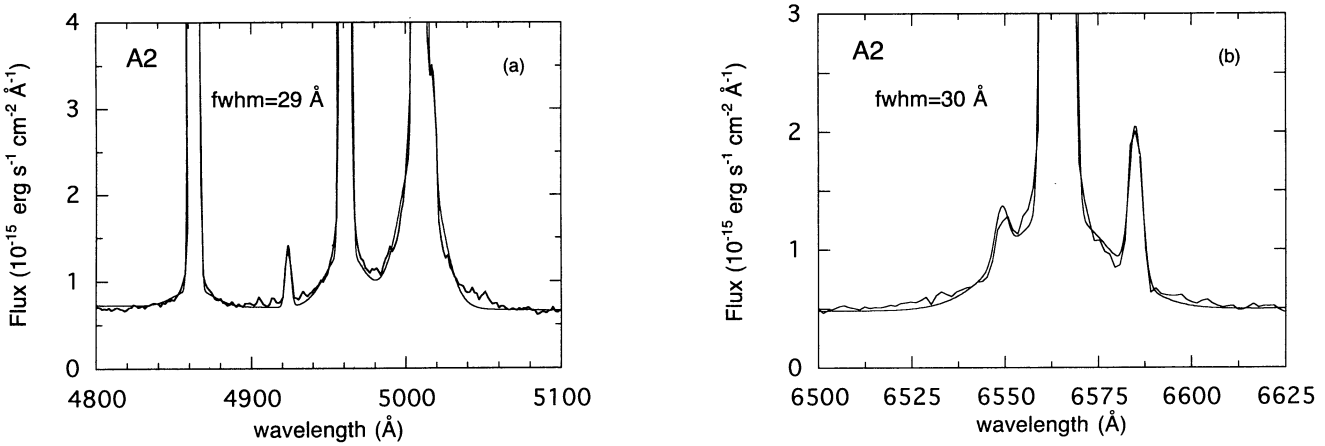

FIG. 15.—Best fits of narrow and broad Gaussians to the (*a*) [O III] λ5007, 4959 and (*b*) Hα lines for the spectra A2. The FWHM of the broad component of Hα is 30 Å, and the relative flux with respect to the narrow component is 3%. The excitation ([O III]/Hα) for the broad component is similar to the excitation for the narrow component.

culation the contributions from the free-free and free-bound transitions of H I, He I, and He II and the two-photon continuum of hydrogen. In $\Delta\gamma_\nu(\mathrm{He}^0, T)$ are included the two discontinuities of the He I at 8195 Å and 8197 Å. The effective recombination coefficient of Hβ has been calculated using the expression given by Pequignot, Petitjean, & Boisson (1991), which is valid at low densities. The helium abundances are taken from § 4.4. The values thus obtained for T_e are $13{,}000^{+2600}_{-2200}$ and $10{,}200^{+1500}_{-1100}$ K, for knots A and B, respectively. These values are significantly lower than those obtained from the collisionally excited line ratios. The reason for this expected result seems well understood from the fact that the nebular continuum emission originates from recombination processes, which weight preferentially low-temperature regions, whereas the collisionally excited line emission is weighted toward higher temperature regions. Peimbert (1967) has suggested that this discrepancy between the two temperature determinations can be explained by the presence of large temperature fluctuations within the nebula, in which case the resulting recombination temperature will always be lower than that obtained from collisionally excited lines.

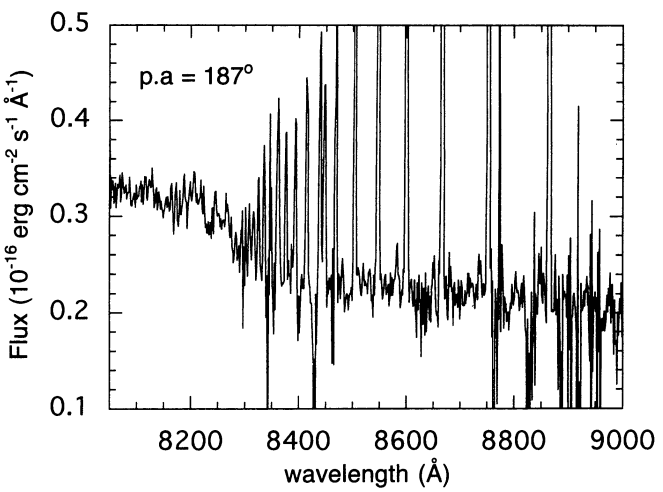

FIG. 16.—An enlargement of the spectrum A2 showing the Paschen discontinuity in emission.

These temperature fluctuations affect the emissivity of the ionic lines and, consequently, the chemical abundances. To compute the effect in the derived abundances, we first obtained the values of the average temperature, T_0, and the rms temperature functions, t_0, defined for an ion X^{+p} as

$$T_0(X^{+p}) = \frac{\int T_e N_e N(X^{+p}) dV}{\int N_e N(X^{+p}) dV},$$

$$t_0^2(X^{+p}) = \frac{\int (T_e - T_0)^2 N_e N(X^{+p}) dV}{T_0^2 \int N_e N(X^{+p}) dV}.$$

Assuming $T_0(\mathrm{H}^+) = T_0(\mathrm{O}^{+2}) = T_0$ and $t_0^2(\mathrm{H}^+) = t_0^2(\mathrm{O}^{+2}) = t_0^2$, we can calculate T_0 and t_0^2 from T_e([O III]) and T_e(Pa) using the expressions given by Peimbert (1967), updated with more recent atomic data (Garnett 1992),

$$T_e([\mathrm{O\ III}]) = T_0\left[1 + \frac{1}{2}\left(\frac{91380}{T_0} - 3\right)t_0^2\right],$$

$$T_e(\mathrm{Pa}) = T_0(1 - 1.67t_0^2).$$

The values we find are 14,600 and 12,200 K for T_0, and 0.064 and 0.098 for t_0^2, for knots A and B, respectively. These large values obtained for t_0^2 in both knots indicate that large temperature fluctuations are present in NGC 2363. These values are really high if we compare them with the mean value of $t_0^2 = 0.03$ recently obtained by Liu & Danziger (1993) for a sample of planetary nebulae. However, these authors also find a few objects with $t_0^2 > 0.1$.

To see the effect of these fluctuations in the calculation of the chemical abundances, we have expanded the ion emission coefficients in a power series. For an ion X^{+p}, the abundance can be calculated to second order as

$$\frac{N(X^{+p}, \lambda_{nn'})}{N(\mathrm{H}^+)} \propto T_0^a e^{b/T_0} \times \left\{1 + \frac{1}{2}\left[a(a-1) + \frac{b^2}{T_0^2} + \frac{2b}{T_0}\right]t_0^2\right\} \frac{I(X^{+p}, \lambda_{nn'})}{I(\mathrm{H}\beta)},$$

where the coefficients a and b depend on the wavelength and the ion, $a(X^{+p}, \lambda_{nn'})$ and $b(X^{+p}, \lambda_{nn'})$.

The effect in the He abundance is quite small (it is decreased by less than 6%), since the temperature dependence of the He emissivity is very small. However, the correction is important for the metallic ions, increasing the corrected abundances with respect to the values obtained in § 4.4; for example, for the total oxygen abundance the increase is a factor 1.6 (0.2 dex) and 2.7 (0.43 dex) for knots A and B, respectively, with respect to the uncorrected value. This increases the difference of the abundances in the two knots.

5.5. *Ionization Structure*

The 15 different spectra extracted provide us with a good sampling for the study of the ionization structure of NGC 2363.

Let us first consider the question whether photoionization by young stars constitutes the main excitation mechanism, since shock heating produced by stellar winds from W-R stars and supernova explosions is also possible. Where shock heating plays an important role, the ratios [O III]/Hβ, [N II]/Hβ, [S II]/Hβ, and [O I]/Hβ are significantly enhanced. We have represented the different spectra in the Baldwin, Phillips, & Terlevich (1981) diagram and found that those line ratios are always compatible with photoionization as the major excitation mechanism. Further support comes from the fact that [O I] emission is *not* detected in knot A. However, in a highly ionized medium the presence of shocks affects mainly the line [O III] λ4363 (Peimbert, Sarmiento, & Fierro 1991). This line is very extended around both knots, but we have failed to find any significant variations in T_e([O III]). However, the FWHM of this line looks larger than that of Hγ; but these widths are close to the limit of our instrumental resolution, and we need better spectral resolution to confirm this important result. If this result is confirmed it would unambiguously confirm the presence of shocks in NGC 2363.

Reddening across the nebula seems to be constant and at a low value. Furthermore, we have not found any correlation between the ratio [O III]/[O II] and C(Hβ), which indicates that the low amount of reddening found, C(Hβ) = 0.2, is likely caused outside the nebula.[11] Otherwise dust mixed with the gas should lead to a correlation between reddening and the ionization structure.

However, there is a variation of the excitation ratio [O III]/[O II]. This ratio has its largest values at A2 and B4 and its lowest values at A1 and B1. In fact, there is a strong north-south asymmetry in the region, which in Figure 10 is seen as a steep fall of the excitation toward the south, while the decrease is much shallower toward the north. This asymmetry is also seen in the Hα image of Figure 1*b*, where it is apparent that NGC 2363 and NGC 2366 II are sharply limited toward the southwest, but diffuse to the northeast; this has a strong correspondence with the distribution of neutral hydrogen as deduced from Figure 2 of Wevers et al. (1990), where the H I distribution in NGC 2366 presents the largest column density to the south of NGC 2363. The [O III]/[O II] ratio is sensitive to the ionization parameter, $U = Q/4\pi r^2 c N_e$, but reasonably insensitive to other parameters which affect the relative emission line intensities (such as the shape of the ionizing continuum and the chemical composition). Penston et al. (1990) give a general recipe for finding U from [O III]/[O II]; using their prescription, we find a range of values $0.003 \leq U \leq 0.03$.

[11] Note that the extinction due to our Galaxy amounts only to $C(\mathrm{H}\beta) \leq 0.05$, according to the maps in Burstein & Heiles (1982).

In knot A, the excitation decreases outwards from the central maximum (Fig. 10*a*), which is coincident with both line and continuum maxima. In knot B, however, the excitation maximum is displaced $\sim 6''$ north of the emission line maximum (Fig. 10*b*), and there is a local minimum at the position of the continuum maximum, where the W-R is located ($\sim 1''.5$ north of the line maximum). This local minimum in the ionization parameter, $U = 0.01$, could be explained by a decrease in the filling factor produced by the W-R wind.[12,13] In effect, we find that there is a positive relationship between the excitation and the equivalent width of Hβ, which means a relationship between the ionization parameter and the evolutionary stage of the region, since EW(Hβ) traces the age of the cluster for a given IMF (Copetti, Pastoriza, & Dottori 1986). Thus the above-mentioned local minimum of U, where the W-R emission is found, can be understood if knot B is older than knot A. This is further supported by the fact that, although the general behavior of EW(Hβ) is similar in both knots, the value at the W-R location is much smaller than at the corresponding location in knot A. All the evidence is in favor of knot B being older than knot A (where no W-R emission is found).

There are no significant variations detected in the total abundances, and the whole region can be characterized by the weighted mean values of 12 + log (O/H) = 7.89, 12 + log (Ne/H) = 7.03, log (N/O) = -1.61, log (S/O) = -1.71, and He/H = 0.08, which correspond to a metallicity $z = 0.00165$ and $y = 0.239 \pm 0.003$. This result suggests that, unlike what is sometimes seen in ring nebulae around W-R stars in our Galaxy (Esteban 1992), the gas in NGC 2363 is not polluted by the W-R star wind. Enhanced N and He have been found in H II galaxies (e.g., NGC 5253; Walsh & Roy 1989), and Vilchez & Esteban (1991) have shown that interstellar material mixed with $\sim 10\%$ enriched material expelled by a W-R star can account for most of the N and He excesses observed in H II galaxies.

From the Hα flux in the spectrum where the W-R feature is detected, we estimated the mass of ionized gas in this area to be $\sim 4000\ M_\odot$. If one W-R star is present, an upper limit to the mass expelled could be $\sim 40\ M_\odot$, which represents 1% of the total mass in gas. Ten percent of $\sim 40\ M_\odot$ equals the mass of N polluted by one WN (using the empirical N yield obtained by Esteban 1992). This $\sim 4\ M_\odot$ of N translates, for our abundances, into log(N/O) = 0.05, which is within the estimated error of the nitrogen abundance.

6. SUMMARY AND CONCLUSIONS

From narrowband Hα imaging and long-slit optical and near-infrared spectroscopy we have derived the main physical properties of the supergiant H II region NGC 2363, which is experiencing a recent violent burst of star formation.

From the Hα image we have obtained a total luminosity of log L(Hα) = 40.15 ergs s^{-1}, a mass of ionized gas of $3 \times 10^5\ M_\odot$, and a total mass for the star cluster of $3.4 \times 10^5\ M_\odot$.

Long-slit optical and near-infrared spectroscopy was obtained at two locations in the nebula, at the brightest core

[12] $U \propto \phi^{2/3}$, where ϕ is the volume filling factor.

[13] Ultraviolet spectra from the *IUE* satellite analyzed by Roy et al. (1992) show a P Cygni–type profile in the line of C IV λ1549 where the entrance aperture is aligned such that emission from the two knots, A and B, is observed, but does not show C IV absorption when only knot A falls within the aperture.

(knot A, at P.A. = 187°) and at 6″ south (knot B, at P.A. = 130°, 185°). We have confirmed the existence of a low-intensity, very broad spectral component under Hα and [O III], previously reported by Roy et al. (1992). This broad emission extends ~500 pc, in both the north-south and east-west directions. The weighted mean value FWHM for the broad component of Hα is ~1300 km s^{-1}, which would imply a kinetic energy of $\sim 3 \times 10^{52}$ ergs.

We have derived the physical conditions of the ionized gas (reddening, electron temperatures, and densities) for 15 different extracted zones in the region. A very low amount of reddening is found, with no significant variations across the region. No significant variation is found in the electron temperatures determined from the nebular to auroral collisionally excited line ratio of [O III]: 16,000 and 15,000 K for knots A and B, respectively. However, electron temperatures derived from the recombination processes resulting in the Paschen discontinuity, calculated in both knots, give much lower values: 13,000 and 10,200 K. This large discrepancy indicates the presence of large temperature fluctuations within the nebula. These fluctuations could be related to the presence of shocks in the region.

The nebular He II λ4686 line is found to be very extended at the two positions, suggesting a very hard radiation field associated with the star formation.

Without taking into account the temperature fluctuations, we have obtained oxygen, nitrogen, sulfur, neon, and helium abundances in 13 different zones, giving weighted mean values of 12 + log (O/H) = 7.89, 12 + log (Ne/H) = 7.03, log (N/O) = −1.61, log (S/O) = −1.71, and He/H = 0.08, which correspond to $z = 0.00165$ and $y = 0.239 \pm 0.003$. We do not find abundance variations within the nebula, including a region where W-R emission bands are discovered. The λ4660 and λ5800 W-R features found in knot B are indicative of WC stars, a fact that, according to recent evolutionary models, is consistent with the low-metallicity derived. The existence of these W-R features gives an age of 3–5 Myr for the region.

It will be important to confirm whether the temperature fluctuations we have found are also present in other H II regions, because they have a direct consequence in the determination of the element abundances. Taken into account, the fluctuations increase the metal abundance by ~0.43 dex and ~0.2 dex (for O/H) for knots B and A, respectively, and decrease the He abundance less than 6%. In this range of O/H, the effect of these fluctuations could be important in the case of the primordial helium abundance. If temperature fluctuations are generally significant in other H II regions, then a revision of computed chemical compositions would be needed, and both the increase of O/H and the decrease of He/H would turn the slope of the y versus O/H regression to steeper values.

The spectrum and physical properties of this region indicate that NGC 2363 is undergoing a violent burst of recent star formation, where stellar winds from W-R stars play an important role.

We are grateful to the Comité Científico Internacional for allocating 5% of the observatory time to the GEFE collaboration. The 4.2 m William Herschel and 1 m Jacobus Kapteyn telescopes are operated by the Royal Greenwich Observatory at the Spanish Observatorio del Roque de los Muchachos of the Instituto de Astrofísica de Canarias. B. Vila-Vilaró kindly provided a program to correct two-dimensional spectral frames for the atmospheric differential refraction. We are also grateful to L. Cuesta for allowing access to his general-purpose analysis software GRAFICOS, which has been extensively used during the course of this work. We acknowledge several conversations with M. Peimbert and M. Edmunds and the comments from the referee, which helped to improve some of the discussion presented in this paper. We acknowledge the use of the Starlink Software Collection of the UK Science and Engineering Research Council for all calibration and measurement of data presented in this paper. This work has been partly financed by DGICYT grant PB91-0531(GEFE) and by NATO grant CRG 920198 for collaborative research.

REFERENCES

Aller, L. H. 1984, Physics of Thermal Gaseous Nebulae (Dordrecht: Reidel)
Arnault, P., Kunth, D., & Schild, H. 1989, A&A, 224, 73
Baldwin, J. A., Phillips, M. M., & Terlevich, R. J. 1981, PASP, 93, 5
Bergeron, J. 1977, ApJ, 211, 62
Brocklehurst, M. 1971, MNRAS, 153, 471
Brown, R. L., & Mathews, W. G. 1970, ApJ, 160, 939
Burstein, D., & Heiles, C. 1982, ApJ, 87, 1165
Campbell, A., Terlevich, R. J., & Melnick, J. 1986, MNRAS, 223, 811
Castañeda, H. O., Vilchez, J. M., & Copetti, M. V. F. 1990, ApJ, 365, 164
Cerviño, M., & Mas-Hesse, J. M. 1994, A&A, 284, 749
Clegg, R. E. S. 1987, MNRAS, 229, 31P
Conti, P. S. 1991, ApJ, 377, 115
Copetti, M. V. F., Pastoriza, M. G., & Dottori, H. A. 1986, A&A, 156, 243
Esteban, C. 1992, Ph.D. thesis, Univ. La Laguna
Filippenko, A. V. 1982, PASP, 94, 715
Fogotto, F., Bressan, A., Bertelli, G., & Chiosi, C. 1994, A&AS, 104, 365
García-Vargas, M. L., Bressan, A., & Díaz, A. I. 1994, in preparation
Garnett, D. R. 1989, ApJ, 345, 282
———. 1991, ApJ, 373, 458
———. 1992, AJ, 103, 1330
Hook, R. N., & Lucy, L. B. 1992, in Science with the *Hubble Space Telescope*, ed. P. Benvenutti & E. Schreier (Garching: ESO), 245
Howarth, I., & Murray, J. 1991, Starlink User Note, No. 50
Kennicutt, R. C., Balick, B., & Heckman, T. 1980, PASP, 92, 134
King, D. L. 1985, La Palma Tech. Note, No. 15
Kurucz, R. 1992, in IAU Symp. 149, The Stellar Populations of Galaxies, ed. B. Barbuy & A. Renzini (Dordrecht: Kluwer), 225
Liu, X. W., & Danziger, J. 1993, ESO Preprint Ser., No. 904
Lucy, L. B. 1974, AJ, 79, 745
Maeder, A. 1990, A&A, 84, 139
McCall, M. L. 1984, MNRAS, 208, 253
Mendoza, C. 1983, in IAU Symp. 103, Planetary Nebulae, ed. D. R. Flower (Dordrecht: Reidel), 143
Moffat, A. F. J. 1969, A&A, 3, 455
Olofsson, K. 1989, A&AS, 80, 317
Osterbrock, D. E. 1989, Astrophysics of Gaseous Nebulae and Active Galactic Nuclei (Mill Valley, CA: University Science Books)
Pagel, B. E. J., Simonson, E. A., Terlevich, R. J., & Edmunds, M. G. 1992, MNRAS, 255, 325
Peimbert, M. 1967, ApJ, 150, 825
Peimbert, M., Peña, M., & Torres-Peimbert, S. 1986, A&A, 158, 266
Peimbert, M., Sarmiento, A., & Fierro, J. 1991, PASP, 163, 815
Peimbert, M., & Torres-Peimbert, S. 1987, Rev. Mexicana Astron. Af., 158, 266
Penston, M. V., et al. 1990, A&A, 236, 53
Pequignot, D., Petitjean, P., & Boisson, C. 1991, A&A, 251, 680
Pérez, E., et al. 1994, in preparation
Richardson, B. H. 1972, J. Opt. Soc. Am., 62, 55
Roy, J.-R., Aube, M., McCall, M., & Dufour, R. J. 1992, ApJ, 386, 498
Roy, J.-R., Boulesteix, J., Joncas, G., & Grundseth, B. 1991, ApJ, 267, 141
Sargent, W. L. W., & Filippenko, A. V. 1991, AJ, 102, 107
Seaton, M. J. 1975, MNRAS, 170, 475
Skillman, E. D., & Kennicutt, R. C. 1993, ApJ, 411, 655
Smith, L. F. 1991, in IAU Symp. 143, Wolf-Rayet Stars and Interrelations with Other Massive Stars in Galaxies, ed. K. A. van der Hucht & B. Hidayat (Dordrecht: Kluwer), 601
Stasińska, G. 1978, A&A, 48, 299
———. 1982, A&A, 66, 257
Terebizh, V. Yu. 1990, Astrophysics, 33, 358
Vilchez, J. M. 1987, Ph.D. thesis, Univ. La Laguna
Vilchez, J. M., & Esteban, C. 1991, IAU Symp. 143, Wolf-Rayet Stars and Interrelations with Other Massive Stars in Galaxies, ed. K. A. van der Hucht & B. Hidayat (Dordrecht: Kluwer), 379
Vilchez, J. M., & Pagel, B. E. J. 1988, MNRAS, 231, 257
Walsh, J. R., & Roy, J.-R. 1989, MNRAS, 239, 297
Wevers, B. M. H. R., et al. 1990, A&A, 66, 505
Whitford, A. E. 1958, AJ, 63, 201
Wilkins, T. N., & Axon, D. J. 1991, TWODSPEC, Starlink User Note, No. 16